POLITECNICO DI MILANO

SCUOLA DI INGEGNERIA INDUSTRIALE E DELL'INFORMAZIONE

CORSO DI LAUREA MAGISTRALE IN ENGINEERING PHYSICS

MID-INFRARED KERR-LENS MODE-LOCKED CHROMIUM-DOPED CHALCOGENIDE LASERS

Supervisor: Dr. Gianluca GALZERANO
Assistant supervisor: Eng. Yuchen WANG

Master Thesis of:
Nicolò MOSCHERA
Matr. 841464

ACADEMIC YEAR 2016-2017

Contents

List of Figures

List of Tables

Acknowledgements

The first thanks goes to Dr. Gianluca Galzerano for being much more than a ”simple” supervisor, showing from the very beginning a human side that few choose to show.
Thanks to Yuchen Wang and Toney Teddy Fernandez for the disinterested help they have given to me every single day of this experience.
A special thanks to my parents, without whom this goal would never have been feasible, and to Francesca for her constant support.
Thanks to my friends, old and new ones, who have filled these years with unique moments.
The last thanks goes to music which, during these five years of scientific notions, has given to me the right amount of levity and serenity to continue my studies.
Superamici 4 evah.

Ringraziamenti

Il primo grazie va a Dr. Gianluca Galzerano per essere stato molto più di un ”semplice” relatore, mostrando fin da subito un lato umano che in pochi scelgono di mostrare.
Un grazie a Yuchen Wang e Toney Teddy Fernandez per il disinteressato aiuto che mi hanno dato in ogni singolo giorno di questa esperienza.
Un grazie speciale ai miei genitori, senza i quali questo traguardo non sarebbe mai stato raggiungibile, ed a Francesca per il suo costante supporto.
Un grazie agli amici, vecchi e nuovi, che hanno riempito questi anni di momenti unici.
L’ultimo grazie va anche alla musica la quale, durante questi lunghi cinque anni di nozioni scientifiche, mi ha fornito quella giusta dose di leggerezza e serenità per continuare gli studi.
Superamici 4 evah.

Abstract

This work is focused on the generation of ultra-short pulse trains by a $Cr^{2+}: ZnSe$ and $Cr^{2+}: ZnS$ Kerr-lens mode-locked lasers.

The best result achieved is for $ZnSe$ host material with 3% output coupler, which demonstrated transform-limited pulse trains as short as 48 fs at 2.4 μm with a repetition rate of 143 MHz and an average output power of 200 mW. Highly results were obtained with the ZnS mode-locked laser, which demonstrated pulse duration of 79 fs with average output power of 250 mW.

The whole characterization of the realized mode-locking laser oscillators is presented with particular attention to the relative intensity noise of the sources.

Sommario

Questo lavoro è focalizzato sulla generazione di treni di impulsi ultra-brevi per mezzo di laser in regime di Kerr-lens mode-locking basati sui cristalli di $Cr^{2+}:ZnSe$ e di $Cr^{2+}:ZnS$.

Il miglior risultato raggiunto è per il il cristallo di $ZnSe$ con un accoppiatore di uscita al 3%, il quale ha dimostrato treni di impulsi limitati per trasformata della durata di 48 fs a 2,4 μm con una frequenza di ripetizione di 143 MHz ed una potenza di uscita media di 200 mW. Altrettanto alti risultati sono stati ottenuti con il laser di ZnS in regime di mode-locking, che ha dimostrato una durata temporale degli impulsi di 79 fs con potenza media di uscita di 250 mW.

L'intera caratterizzazione degli oscillatori laser in regime di mode-locking realizzati viene quì presentata con particolare attenzione al rumore relativo di intensità delle sorgenti.

Introduction

Until now middle-infrared (mid-IR) lasers are broadly demanded for their different applications in fields like sensing, spectroscopy of gas molecules like HF and CH_4 and both industrial and medical processes. Cr- and Fe- ions result to have a large efficiency that allows output power in the order of watts with a broad band also operating at room-temperature: for these and other reasons, like the four-level structure, these materials are referred to as the "Ti:Sapphire of the mid-IR". Rare-Earth and transition-metal ions doped crystals are the most used for efficient mode-locked laser resonators, and the typical host materials is a chalcogenide matrix.

The wide overview in the mid-IR sources makes a more focused analysis necessary. Mid-IR sources (Fig. 1) are in facts really heterogeneous for what concern performances and optical characteristics, and our work is located under the first branch of the scheme, under the voice "solid state/rare earth/pulsed ns-fs" precisely.

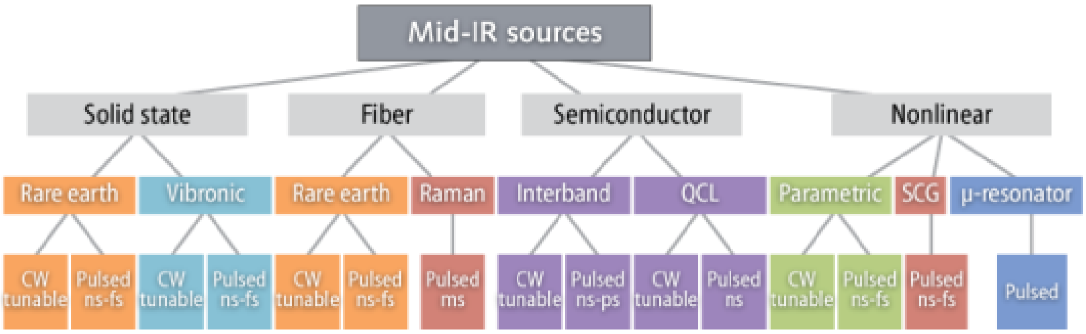

Figure 1: Different types of mid-infrared light sources and their corresponding operation modes.

We developed new laser sources based on Cr-doped ZnS and ZnSe crystals for femtosecond pulse generation in the spectral region of 2-3 μm because our goal is to realize mid-infrared frequency comb for spectroscopy investigation. The best result achieved is for $ZnSe$ host material with 3% output coupler, which demonstrated transform-limited pulse trains as short as 48 fs at 2.4 μm with a repetition rate of 143 MHz and an average output power of 200 mW. Highly results were obtained with the ZnS mode-locked laser, which demonstrated pulse duration of 79 fs with average output power of 250 mW.

Ultra-short pulse generation means a good compensation of the group velocity dispersion in the experimental set-up and a broad band emission spectrum. Mode-locking dynamics result to be the most efficient and in particular the Kerr-lens mode-locking that allows to exploit non-linearities inside particular active media in order to modulate gain and losses and get a stable pulsed regime. Our analysis will in facts starts from mode locking theory.

In particular this thesis is structured as following:

1. First chapter analyzes mode-locking regime from both the two main point of view: frequencies and time domains. Starting from theory, the work will highlights the differences between active and passive mode-locking methods, focusing on the Kerr-lens one and on the different dispersion compensation methods.
2. Second chapter introduce the main crystals used in the mid-IR region, starting from rare-earth and transition-metal ions doped crystals to the main solid state commercial lasers. Then, chalcogenide host materials will be analyzed in a more focused way, together with their optical properties.
3. Third chapter will first explain our set-up system for the realization of an efficient $Cr^{2+}:ZnSe$ and $Cr^{2+}:ZnS$ laser, presenting all the technical parameters and the practical arrangements. Then, all the experimental results about these lasers will be presented, focusing on 150 MHz and 250 MHz configurations with 3% output coupler and, for some case, also 1% output coupler.

Chapter 1

Ultra-short pulse trains generation

Generation of ultra-short pulse trains has been improved a lot since the first time it was developed 40 years ago [1]. Applications in fast chemical or electronic processes made this technique grow up, making it essential in ultra-precise spectroscopic measurements. Once the frequencies of the longitudinal modes that constitute the pulse trains are perfectly controlled the mode-locked laser become an Optical Frequency Comb [2]. The advantage of this "ruler" is to determine all the frequency components of an unknown light with high precision. For these and several others issues it is important to investigate accurately this field of optical science, in order to understand how it is possible to generate a stable pulsed source.

1.1 Mode-locking regime

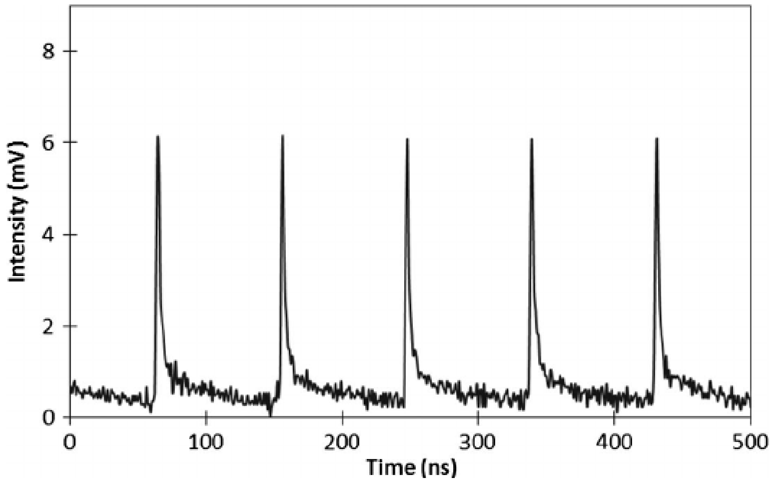

Figure 1.1: Intensity (I) vs time in a mode-locking regime. Copyright [1].

Mode-locking is a particular regime where a laser is forced to oscillate in different longitudinal modes which have a perfectly determined phase-relationship. The laser's output is a train of pulses whose temporal duration, τ_p, is equal to the inverse of the bandwidth of oscillating modes and the period, T_r, equals the transit time of the light inside the resonator. Each round-trip, the pulse, thanks to a modulation synchronous with the round-trip time, can shrink passing through the active media, enlarging its bandwidth and reaching a steady-state where no more shortening processes are allowed[3].
Let's see in detail the theory behind this process and the various experimental techniques developed.

1.1.1 Frequency domain description

Consider the relation between two adjacent modes in a set of $2n+1$ longitudinal modes [1]. This relationship can be written as

$$\varphi_l - \varphi_{l-1} = \varphi \tag{1.1}$$

This equation shows the phase locking between longitudinal modes. The electric field can be written as

$$E(t) = \sum_{-n}^{+n} E_0^l exp\left\{j[\omega_0 + l\Delta\omega]t + l\varphi\right\} \tag{1.2}$$

where the central frequency is ω_0 and $\Delta\omega$ is the difference interval between adjacent modes[1]. In a more compact way, the electric field can be written as

$$E(t) = A(t)exp\left\{j\omega_0 t\right\} \tag{1.3}$$

where

$$A(t) = \sum_{-n}^{+n} E_0^l exp\left\{jl(\Delta\omega t + \varphi)\right\} \tag{1.4}$$

In this way we can isolate the time dependent amplitude and study its time behavior. Changing the time reference into t' such that $\Delta\omega t' = \Delta\omega t + \varphi$, eq. 1.4 becomes

$$A(t') = \sum_{-n}^{+n} E_0^l exp\left\{jl(\Delta\omega t')\right\} \tag{1.5}$$

Summing the geometrical progression (with ratio $e^{j(\Delta\omega)}$) the amplitude becomes

$$A(t') = E_0 \frac{sin[(2n+1)\Delta\omega t'/2]}{sin[\Delta\omega t'/2]} \tag{1.6}$$

For sure intensity ($I(t')$) is proportional to $A(t')^2$, whose equation is

$$A(t')^2 = E_0^2 \frac{sin^2[(2n+1)\Delta\omega t'/2]}{sin^2[\Delta\omega t'/2]} \tag{1.7}$$

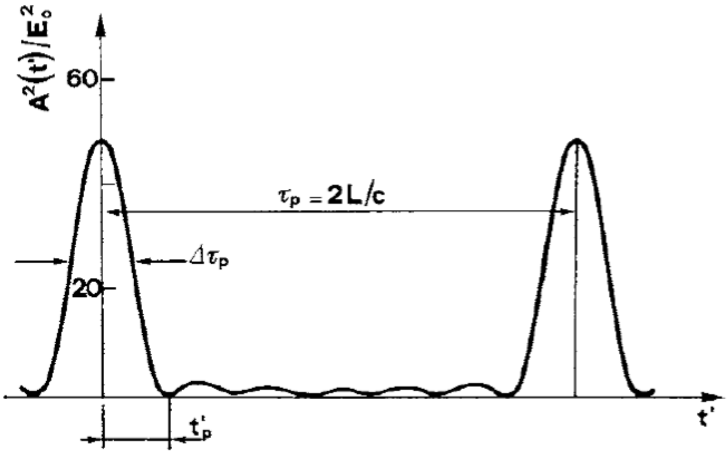

Figure 1.2: Squared amplitude vs time in mode-locking regime, with 7 oscillating modes with equal amplitude E_0. Copyright [1].

Figure 1.3: Mode amplitudes against frequencies.

Fig. 1.2 gives a graphical representation of equation 1.7 assuming only 7 oscillating modes.
It's easy to see from Eq. 1.7 that the pulse's maximum takes place when the denominator becomes zero, as result outcome of the modes' interference (Eq. 1.1). Considering the time where the first pulse ($\Delta t'/2 = 0$) and the second ($\Delta t'/2 = \pi$) take place, we can retrieve the relation between two successive pulses $T_r = 2\pi/\Delta\omega = 1/\Delta\nu$ (Eq. 1.9). In order to obtain a good estimation of the pulse width depending to the number of oscillating modes in the cavity, we can notice that the main central part of the sin^2 can be approximated with a triangle where its $FWHM = base/2$. The first zero of the numerator of Eq. 1.7 is set for t' that satisfies $[(2n+1)\Delta\omega t'/2] = \pi$. This basic approximation allow us to write

$$\tau_p = \frac{2\pi}{(2n+1)\Delta\omega} = \frac{1}{\Delta\nu} \tag{1.8}$$

where $\Delta\nu$ is the oscillating bandwidth under the gain curve (Fig. 1.3).

1.1.2 Time domain description

Equation 1.1 implies a separation of T_r seconds between two consecutive pulses given by

$$T_r = \frac{2\pi}{\Delta\omega} \tag{1.9}$$

where $\Delta\omega$ is the separation in frequency between two adjacent modes. Since $\Delta\omega = \frac{2\pi c}{2L}$, where the cavity length is L, it becomes obvious that the time separation between pulses is the round trip time of the cavity, analytically expressed by $T_r = 2L/c$. It's important to highlight that the pulse's duration τ_p is much shorter than the separation time between consecutive pulses, usually 3 or even 6 orders of magnitude shorter. Describing this phenomenon in the above way, with a train of pulses of duration τ_p and separation time T_r, we are referring to the *time-domain picture*.

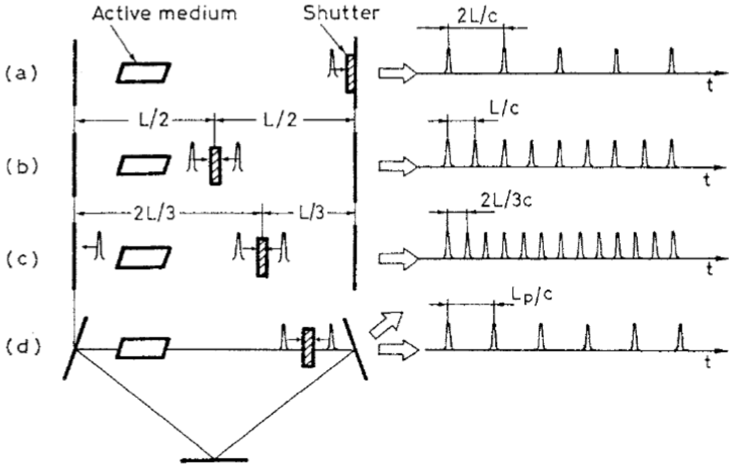

Figure 1.4: Mode-locking with a fast cavity shutter. Position of the shutter is crucial in order to determine the repetition rate. (a), (b) and (c) are different configurations in a linear cavity. Figure (d) shows up a ring cavity configuration. Copyright [1].

Referring to Fig. 1.4, one of the possible practical approach can be to induce modulated losses putting a fast shutter inside the cavity, forcing the pulsed regime. If this shutter opens periodically with period $T = 2L/c$ and if the opening time is similar to the time duration of the noise pulse of the beam propagating inside the cavity, only this pulse will survive and this will favors mode-locking regime described in Fig. 1.4a. In the same way it is easy to notice that if the shutter is placed at the center of the resonator and periodically opened with period $T = L/c$, two pulses will survive inside the cavity (Fig. 1.4b). If the shutter is placed at a distance $L/3$ from one mirror and opened with period $T = 2L/3c$, three pulses will propagate (Fig. 1.4c). Fig. 1.4a refers to the *fundamental modelocking* situation with a repetition rate equal to $\Delta\nu_0 = c/2L$. Fig. 1.4b and Fig. 1.4c, having $\Delta\nu = 2\Delta\nu_0$ and $\Delta\nu = 3\Delta\nu_0$ respectively, are sometimes referred to as *harmonic modelocking* situation. Fig. 1.4d is, instead, a completely different configuration called *ring configuration* and the repetition rate in this case is completely independent from the shutter position.

A deeper analysis is given by the newly developed $ABCD$ matrix formalism. It starts from the basic description of laser beams under Gaussian paraxial approximation, applying it also for the time description. Associating the pulse-width to the spot size and the chirp to the wavefront curvature in the spatial $ABCD$ formalism and than applying it to the principal elements that take part in the mode-locking implementation (defining matrix element for GVD, self-phase modulation and both amplitude and frequency modulations), we are able to obtain immediately a steady-state pulse-width and its corresponding chirp [4].

1.2 Mode locking methods

As all others processes, mode-locking regime can be implemented in different ways:

1. Active mode-locking
    - amplitude modulation (AM)
    - frequency modulation (FM)
2. Passive mode-locking
    - slow saturable absorber
    - fast saturable absorber

Next subsections will then analyze all these methods and discuss all the implementations that have been developed, giving special attention to the fast saturable absorber method which has many similarities with the Kerr-lens one that we will exploit.

1.2.1 Active mode-locking

Both AM and FM-type mode-locking have been investigated by Harris and McDuff in their works ([5], [6]), but also other innovative approaches, like Kuizenga and Siegman ones ([7]), have been made, giving us a powerful instrument by which estimate pulse's duration. The principle behind active mode-locking is the modulation of a parameter thanks to an active region added into the laser cavity. By controlling the resonator losses (AM case) or the phase-match (FM case) it's possible to change the stability of the laser and turns the DC regime into a pulsed one.

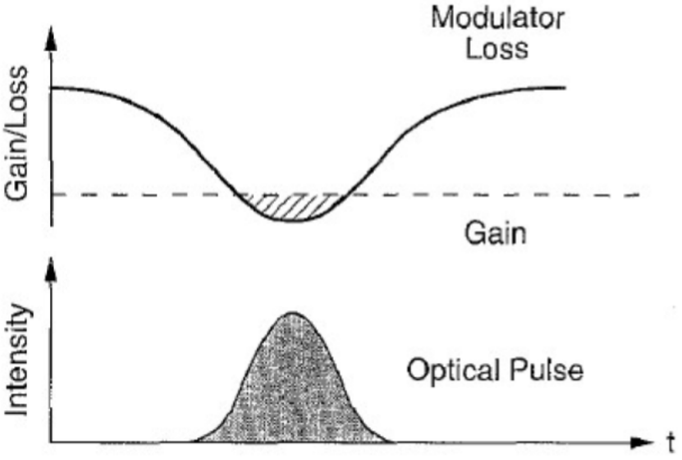

Figure 1.5: Working principle of AM mode-locking. It's possible to see the pulse formation due to the net gain created by the losses modulation. Copyright [8]

AM mode-locking

The basic concept of AM mode-locking is the modulation of cavity losses through an additional variable modulator (like a Pockels cell or an acousto-optic modulator). This modulator in facts creates a "window" where, at each step, the laser sees a net positive gain. This round-trip gain allows the formation of one pulse per period as shown in Fig. 1.5. To understand pulse formation we can consider a parabolic shape approximation for the pulse's electric field

$$E(t) = E_0 \left(1 - \frac{t^2}{\tau^2}\right) \tag{1.10}$$

where E_0 and τ are peak amplitude and time constant of the shape respectively. We can assume that the modulator, where the beam passes through, gives an output similar to

$$T = 1 - m(1 - cos\omega_m t) \tag{1.11}$$

that is, with Taylor expansion around the central value,

$$T \cong 1 - \frac{m(\omega_m t)^2}{2} \tag{1.12}$$

where ω_m is the modulation frequency and m a numerical factor. Passing inside the modulator, the pulse will change its shape according to

$$E(t) = E_0 \left(1 - \frac{t^2}{\tau'^2}\right) \tag{1.13}$$

where the relation between the two times constant is

$$\frac{1}{\tau'^2} = \frac{1}{\tau^2} + \frac{m\omega_m^2}{2} \tag{1.14}$$

In the end, as a consequence, the reduction in pulse duration can be estimated with

$$\frac{\Delta\tau}{\tau} = \frac{m\omega_m^2\tau^2}{4} \tag{1.15}$$

Each round-trip the pulse will shrink in the time domain, reaching after several round-trips a steady-state where no more shortening processes will be allowed. This is the main limitation to pulse bandwidth and the way in which finite bandwidth of the active medium influences the steady-state duration is different according to the different broadening processes (homogeneous or inhomogeneous). For inhomogeneous lines the oscillating bandwidth $\Delta\nu_L$ tends to cover all the gain bandwidth $\Delta\nu_0^*$ and, assuming a Gaussian amplitude profile, we can estimate pulse duration with

$$\Delta\tau_p \cong 0.441/\Delta\nu_0^* \tag{1.16}$$

Differently, for an homogeneous line the mechanism is pretty different and drives the pulse through shorter time duration according to

$$\Delta\tau_p \cong 0.45/(\nu_m\Delta\nu_0)^{1/2} \tag{1.17}$$

where ν_m is the frequency of the modulator that is equal to $c/2L$ for fundamental mode-locking.

FM mode-locking

Differently from the previous case, FM mode-locking is easier to be understood looking it trough the frequency domain because it is based on the cavity modes phase-matching. Let's take into account a different type of modulator, which has a modulated refractive index with ω_m as frequency modulation, and place it at one end of the resonator. A phase contribution will be added to any cavity mode and this shift will be

$$\varphi = \left(\frac{2\pi L'}{\lambda}\right) n(t) \tag{1.18}$$

where L' is the actual cavity length and $n(t)$ is the time-varying refractive index. These phase modulated modes will exhibit sidebands which, when $\omega_m = \Delta\omega$, will have the frequency exactly equals to its neighbor's one. This is a phase-locking form as 1.1 one, although the condition is different. According to Fig. 1.6, in the time domain picture two pulsed regimes, and then two different mode-locking regimes, will be established: the former happens when the pulse passes through the modulator at each minimum of the refractive index (solid line), the latter at its maximum (dotted line). Since the effective cavity length is

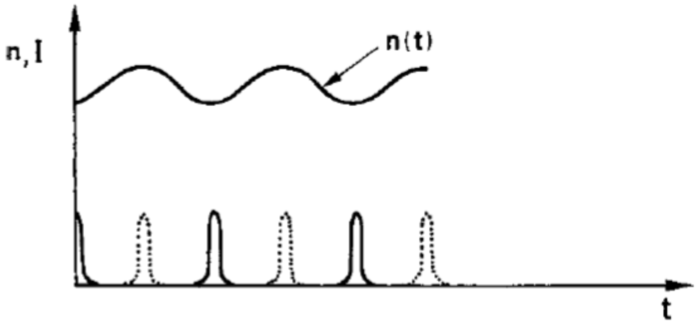

Figure 1.6: Time behaviour of refractive index and pulse formation in FM mode-locking. Copyright [1].

$$L'_e = n(t)L' \tag{1.19}$$

it turns out that this picture results equivalent to an ideal cavity where the length is modulated not by a modulator but by a mechanical system oscillating at ω_m applied to one of the mirror, which can change physically its geometrical length.

Because of the extreme complexity of the mechanical systems needed in order to implement such model, that requires high synchronizing precision, passive techniques could present a more practical solution [8].

1.2.2 Passive mode-locking

Passive mode-locking method can boast the shortest collection of pulses generation, allowing us to reach pulse duration of few optical cycles ($10fs$ at $0.8\mu m$). The main concept behind all passive processes that has to be understood is that the pulse self-modulates itself propagating inside the resonator. What changes is the type of medium that allow such a modulation. In the next paragraphs, two macro-classes of passive mode-locking will be threaten: slow and fast saturable absorbers [8].

Slow saturable absorber

Slow saturable absorbers are nothing but lossy elements which saturate when the power of the input radiation is above a certain threshold value, behaving like transparent media. The peculiarity is that, thanks to the introduction of losses in the CW regime, this process favors the generation of pulsed ooperation. Of course, a slow saturable absorber element can not recover its absorption as fast as the pulse passage, so it is not able to generate much shorter pulse respect to its own recovery time. However, recent studies showed that generation of pulses on picoseconds scale is possible, even if the absorbing element has a relaxation time belonging to the nanosecond scale [9]. An in-depth analysis [10] showed that this can be possible due to a dynamic saturation of the gain: the absorber will absorb the leading part of the pulse, while the trailing one will be subjected to losses due to the gain depletion. Every round-trip both loss and gain recover, and this makes the pulse "wings" get shorter and the peak get higher during each round-trip cycle, allowing shorter pulse formation. In Fig. 1.7 we can see the dynamics of this process.

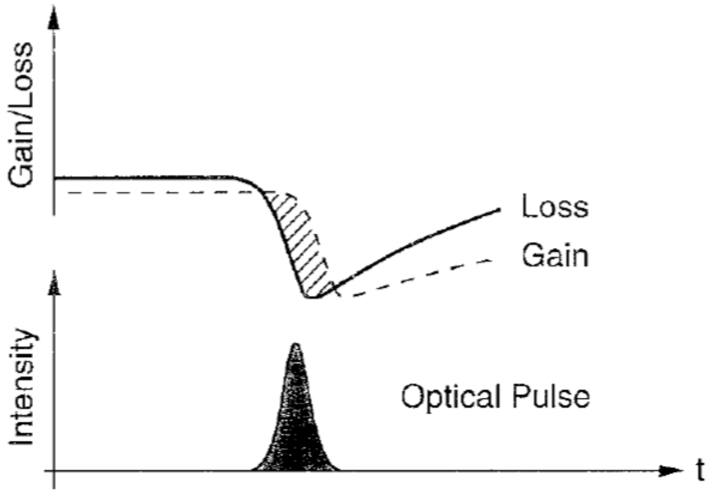

Figure 1.7: Pulse-shaping gain and loss dynamics for slow-saturable absorber mode locking. Copyright [8].

When pulse duration is really short (much more than the recovery time) it's possible to use the following rate-equations:

$$l_a(t) = l_i exp\left(-\sigma_a \int_{-\infty}^{t} |E(t)|^2 dt\right) + l_0 \tag{1.20}$$

$$g(t) = g_i exp\left(-\sigma_g \int_{-\infty}^{t} |E(t)|^2 dt\right) \tag{1.21}$$

where l_0 are the non-saturable losses, σ_a and σ_g are the absorber and gain cross-sections, while l_i and g_i are the initial values of the loss and gain. Analyzing Eq. 1.20 and 1.21 we can see two conditions that will assure a good mode-locking performance: the first is for $l_i > g_i$, which allows to introduce losses in the propagation of the pulse's tails (the requirement is that the absorber recovers faster than the gain), while the second is for $\sigma_a > \sigma_g$ and it assure more gain for the central part of the pulse. More detailed studies about this second condition, like conventional implementation methods, can be found in New and Haus work [11].

We can notice that the losses the pulses acquire inside their tails traveling trough the resonator are not dependent by the pulse-width, but only by the

pulse energy. Differently, the modulation slope is pulse-width dependent (since net gain windows narrows proportionally), therefore we can describe it with $T = 1 - m_s(t^2/\tau^2)$.
The shortening process can be described by the pulse-width decrease per pass, starting from $1/\tau'^2 = 1/\tau^2 + m_s/\tau^2$, that is

$$\frac{\Delta\tau}{\tau} = \frac{m_s}{2} = const. \tag{1.22}$$

For sure this is a dynamic system that will reach a steady-state, and the first analytical description of such a steady-state was proposed by Haus [11]. This formula, presented just below

$$\left[g(t) - l_a(t) - l_0 + i\Psi + \frac{l_0}{\omega_g^2}\frac{d^2}{dt^2} + t_D\frac{d}{dt} \right] E(t) = 0 \tag{1.23}$$

and better known as "steady-state master equation", takes into account all therms playing a fundamental role in this physical process, like single-pass gain (g) and losses (l_a), non-saturable loss (l_0), gain bandwidth (ω_g), timing shift (t_D), optical phase change ($i\Psi$). If both $g(t)$ and $l_{a(t)}$ are expanded to second order in $\int_{-\infty}^{t} |E(t)|^2 dt$, the solution can be written as

$$E(t) = E_0 sech(t/\tau) \tag{1.24}$$

where τ is described by

$$\tau = \left(\frac{1}{\omega_g}\right)\left(\frac{4}{\sigma_a W}\right)\left(\frac{l_0}{l_i}\right)^{\frac{1}{2}} \tag{1.25}$$

and $W = \int_{-\infty}^{+\infty} |E(t)|^2 dt$ is the photon density of the pulse and l_0/l_i is the ratio between DC and saturable absorber losses. Putting back this solution into Eq. 1.23 it's finally possible to find a new equation depending on E_0, Ψ and t_D. Many consideration could be made, but the meaning is just to give an idea of the powerful instrument that Haus created, giving us the possibility to describe analytically the interaction between all these phenomenon like Self-Phase Modulation (SPM), Self-Amplitude Modulation (SAM) and Group Delay Dispersion (GDD) that take part in the pulse generation. Of course this treatment can be applied to further mode-locking process like fast saturable absorber and, like our case, Kerr-lens mode-locking.

Fast saturable absorber

Differently from the previous case, fast saturable absorber responds instantaneously to an intensity change, and this allows to recover its absorption in a time shorter than the pulse time-duration [8]. As we can see in Fig. 1.8, the

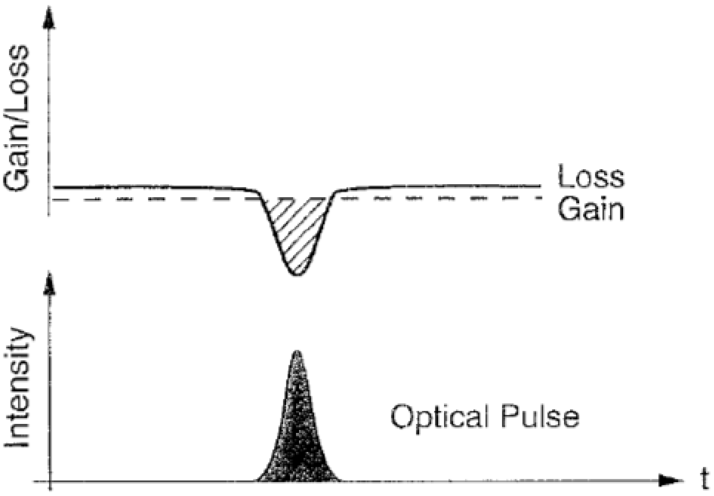

Figure 1.8: Pulse formation for a fast saturable absorber. Copyright [8].

pulse-shape is formed by the net gain and both the edges of the pulse are cut thanks to the fast absorption recovery.

A detailed treatment about fast saturable absorber mode-locking that follows the time-domain approach can be found in Ref.[12]. Here, each component belonging to the experimental set-up is analyzed in order to predict its impact on the electric field propagation and, in the end, on the pulse formation. In order to be more concise, we will follow a qualitative approach.

Let's take into account an absorber characterized by a short absorption recovery time (shorter than the pulse duration) and a low saturation intensity. I_s will be the saturation intensity of the absorber, while I the intracavity beam intensity. For $I >> I_s$ it holds

$$2\gamma_t = 2\gamma - 2\gamma'(I/I_s) \tag{1.26}$$

where γ_t is the round-trip loss, γ and γ' the unsaturable and low-intensity single-pass loss respectively [1]. As Fig. 1.9 shows, we're supposing an absorber placed in contact with one of the mirrors. The two waves propagating inside the resonator will have a completely random phase and the intensity will be characterized by random peaks. For low intensity peaks the saturated round-trip gain (g_0') will approximately be equal to γ, while more energetic peaks will see less attenuation inside the absorber as consequence of the absorber saturation. After many round-trips, if some conditions are satisfied, the pulse can easily grow up, giving a train af pulses on the output (Fig. 1.8) with a certain repetition-rate depending on the cavity length. The average power will increase respect to the CW case and the term g_0' will become smaller than γ (unsaturable loss). Referring to Fig. 1.8, between t_1 and t_2, the pulse tails will see more losses while the peak a net gain, making the pulse shorter each round-trip until an equilibrium is reached (in the steady state condition). The pulse width, in the steady state

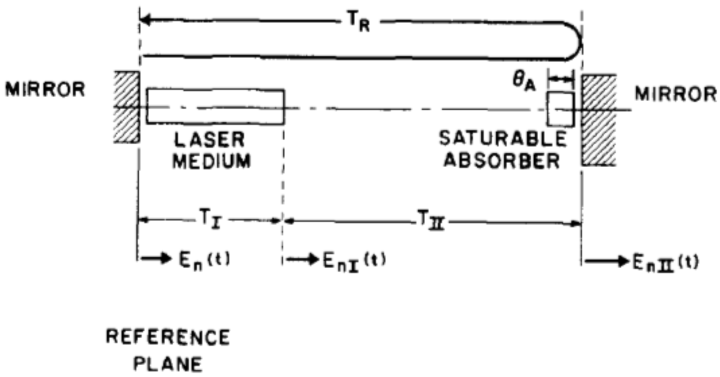

Figure 1.9: Experimental set-up for a fast saturable absorber mode-locking. Copyright [12].

condition, results to be

$$\tau_p \cong \frac{0.79}{\Delta\nu_0}\left[\frac{g_0'}{\gamma'}\right]^{\frac{1}{2}}\left[\frac{I_s}{I_p}\right]^{\frac{1}{2}} \tag{1.27}$$

where $\Delta\nu_0$ is the FWHM and I_p the intensity of the peak.

For what concern the absorber, we can model it like a two level system which has a certain value of saturation, an intensity threshold over which the input beam becomes "transparent". This level is given by

$$I_s = \frac{h\nu}{2\sigma\tau} \tag{1.28}$$

where h is the Plank constant, ν the frequency of the radiation, σ the cross-section for the absorption, τ the life-time of the upper-state of the system. Since τ is typically in the order of few ps, we can have low values of saturation intensity only with pretty large values of the cross-section ($\sim 10^{-16}$). The most commonly used materials with these characteristics are fast dye solutions or semiconductors built with long chain of $(-CH = CH-)_n$. A work about self mode-locking lasers with saturable absorber can be found in bibliography (Ref. [13]).

An easy way to get a passive mode-locking regime exploiting the fast saturable absorber dynamics is to use the so called SESAM (Semiconductor Saturable Absorber Mirror) instead of one of the common mirrors constituting the cavity (Ref. [14] and [15]).

1.3 Kerr-lens mode-locking

As we said, passive mode-locking technique is really powerful in order to generate train of pulses. It is the most efficient way to generate the shortest pulses: active techniques, in fact, can achieve pulsed regime thanks to an externally driven modulation of the optical path, an this is much slower compared to the fast mechanism that characterizes passive techniques with saturable absorbers [16]. Passive techniques have been developed and one of those is the Kerr-lens method, which use Kerr-lens effect to create induced modulation losses inside the resonator. The enormous advantage is that, since this method does not act on population inversion like the absorber case, it can be used for generation of pulses in a wide range of wavelengths. Let's see it in detail.

1.3.1 Kerr-lens effect

Intense lasers are subjected to a self-focusing effect inside non-linear media (which is, in most cases, the active medium), and this is due to the index of refraction dependence by the intensity [17]. This effect will change the spatial profile of the input beam and introducing for example an intracavity aperture inside the resonator it's possible to generate intracavity losses which will depend on the input power. In facts, the more power we have, the more focused the beam will be, according to

$$n = n_0 + n_2 I \tag{1.29}$$

where n_2 is a positive term derived by Taylor expansion. An intuitive representation of this process is shown in Fig. 1.10.

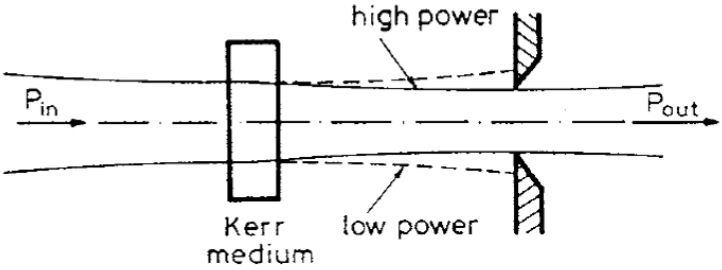

Figure 1.10: Hard aperture Kerr-lens mode-locking. Copyright [1].

Thanks to the quasi-instantaneous response of the Kerr non-linearity, due to the deformation of the atom's electrons cloud in the crystal, the amplitude modulation created by the self-focusing process can simulate the ultrafast saturable absorber and, consequently, generate pulses in the order of fs time duration.

1.3.2 Hard and soft aperture mode-locking

Two different methods of Kerr-lens mode-locking have been built: hard aperture and soft aperture. All these two processes use Kerr non-linearity to introduce modulated losses in the resonator, but the set-up is different. Let's start from the hard aperture case, which we've already met in Fig. 1.10.

Hard aperture

Let's assume a Gaussian shape for the intensity profile of the laser beam inside the resonator: in the central region the Kerr-effect will be more intense and the variation of refractive index inside the active region will be stronger. Intensity, for a Gaussian beam, is

$$I = I_p exp\left[-2\left(\frac{r}{w}\right)^2\right] \tag{1.30}$$

where I_p is the intensity of the peak and w is the spot-size. The pulse, traveling trough the Kerr medium for a distance l, will acquire a non-linear phase according to

$$\delta\phi = \frac{2\pi l\delta n}{\lambda} = \frac{2\pi l n_2 I_p}{\lambda} exp\left[-2\left(\frac{r}{w}\right)^2\right] \cong \frac{2\pi l n_2 I_p}{\lambda}\left[1 - 2\left(\frac{r}{w}\right)^2\right] \tag{1.31}$$

which means, to the first order ($\delta\phi \propto -(r/w)^2$), that the Kerr medium responds to a Gaussian input beam as a spherical lens and the beam becomes focused by Kerr-effect. This phenomenon is called $self-focusing$.

Now, if we imagine to place an hard aperture, like an iris, after the Kerr medium, we can notice that the more the intensity is high the more the beam will focus thanks to the Kerr-effect. This means that high intensity peak will pass through the diaphragm without any relevant losses. This leads to a strong tendency towards the pulsed regime rather than the continuous one, which will experience much weaker self-focusing effect and will be subjected to higher losses. For this particular dynamic, mode-locking that exploits self-focusing process induced by a Kerr medium is really similar to fast saturable absorber method.
A deeper analysis on hard aperture mode-locking, with a correlated analytical study for the efficiency estimation, is given by Ondřej Haderka in Ref. [18].

Soft aperture

The so called soft aperture technique is even more interesting and allows us to reach the same effect of the hard aperture case without the insertion of the diaphragm. Assuming that the previous analytical treatment still holds for the self-focusing, the main difference is that we're not looking at the situation with less loss, but at the one with more gain. As we said before, the self-focusing effect shrinks the laser beam. Now, if the pump beam has beam spot-size slightly smaller than the intracavity laser one, the peaks that, thanks to self-focusing effect, focus better inside the media will have a better alignment with the pump beam, and this will lead to an higher gain. If we have total losses comparable to the unfocused gain, the peaks will be amplified by net gain until an equilibrium is reached. This steady-state will depend on SAM, SPM and GVD. In order to achieve a large efficiency, it's better to operate near one of the two stability

limits: for hard aperture it's better to operate close to the longer cavity length stability limit, for the other case close to the shorter one.
For optimization and analytical derivation, in the case of $Ti : Al_2O_3$ Kerr active medium, refer to Ref. [19], [20].

1.4 Group-velocity dispersion management for ultra-short pulse generation

Pulse formation can not be achieved if we can not manage and control the propagation of the laser beam inside the resonator. During the propagation inside the laser resonator, the pulse will acquire a certain phase shift and this will compromise mode-locking regime. For this reason a dispersion management and compensation is needed. In this section we will discuss the main issues that have to be taken into account and how to operate in order to generate a stable mode-locking, achieving the shortest pulse duration.

1.4.1 Second and third order effects

Second and third order effects needs a more focused consideration, and concepts like phase velocity and group delay dispersion will be analyzed.

Phase velocity

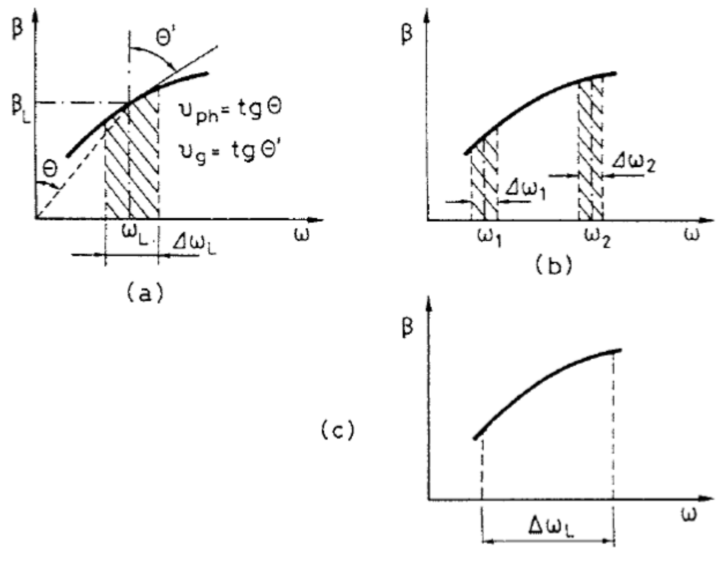

Figure 1.11: (a) Phase and group velocity in dispersive medium; (b) dispersion in time delay for two pulses of carrier frequencies ω_1 and ω_2; (c) group velocity dispersion for a pulse of large oscillation bandwidth $\Delta\omega_L$. Copyright [1].

Let's take into account a plane and linearly polarized monochromatic wave with frequency ω that is propagating along the z axis of a medium. Assume the electric field

$$E(z,t) = A_0 expj(\omega t - \beta z) \tag{1.32}$$

where A_0 is a constant amplitude and β the propagation constant. The so-called *dispersion relation* $\beta = \beta(\omega)$ is a typical characteristic of the material. Considering that the total phase is $\phi_t = \omega t - \beta z$, the velocity of a phase front will be the term that satisfies the relation $d\phi_t = \omega dt - \beta dz = 0$, that is

$$v_{ph} = \frac{dz}{dt} = \frac{\omega}{\beta(\omega)} \tag{1.33}$$

Group velocity and GVD/GDD

Now, let's consider a pulse with frequency centered in ω_L and spectral bandwidth $\Delta\omega_L$. Assuming that the variation of $\beta(\omega)$ over $\Delta\omega_L$ is small enough, we can linearize the relation around ω_L:

$$\beta(\omega) = \beta_L + \left(\frac{d\beta}{d\omega}\right)_{\omega=\omega_L} (\omega - \omega_L) \tag{1.34}$$

where $\beta_L = \beta(\omega_L)$. As a consequence, we can write the electric field as

$$E(t, z) = A\left[t - \left(\frac{z}{v_g}\right)\right] \exp[j(\omega_L t - \beta_L z)] \tag{1.35}$$

where A is the amplitude of the pulse and the exponential term is the carrier wave.
Group velocity v_g is given by

$$v_g = \left(\frac{d\omega}{d\beta}\right)_{\beta=\beta_L} \tag{1.36}$$

or

$$v_g^{-1} = \left(\frac{d\beta}{d\omega}\right)_{\omega=\omega_L} \tag{1.37}$$

Looking at 1.36 and 1.33 we can notice that phase and group velocity are generally different. The pulse, in fact, is moving with an overall velocity, the group velocity, through the length of the medium, and it will be subjected to a time delay, respect to the phase front moving at phase velocity, given by

$$\tau_g = \frac{l}{v_g} = l\left(\frac{d\beta}{d\omega}\right)_{\omega_L} = \phi'(\omega_L) \tag{1.38}$$

The problem of this approximation is that, when the pulse spectral bandwidth $\Delta\omega_L$ is large, the assumption of small variation will not be valid anymore and we need to take into account higher order terms.

Now, let's consider the relationship between phase ϕ and frequency ω and expand it as

$$\phi = \phi_L + \left(\frac{d\phi}{d\omega}\right)_{\omega_L}(\omega - \omega_L) + \frac{1}{2}\left(\frac{d^2\phi}{d\omega^2}\right)_{\omega_L}(\omega - \omega_L)^2 \tag{1.39}$$

where

$$\phi = \beta z \tag{1.40}$$

and

$$\phi_L = \beta_L z \tag{1.41}$$

The time delay of the two frequency components ω_1 and ω_2 of the pulse, traveling inside a dispersive medium with phase relation β, centered frequency at ω_L and spectral bandwidth $\Delta\omega_L$, could be written as

$$\Delta\tau = \phi'(\omega_2) - \phi'(\omega_1) \cong \phi''(\omega_1) \times (\omega_2 - \omega_1) \tag{1.42}$$

In this case we can approximate the time delay between the fastest and the slowest frequency components as

$$\Delta\tau_d \cong |\phi''(\omega_L)|\Delta\omega_L \tag{1.43}$$

where $\phi''(\omega_L)$ is the *group delay dispersion* (or *GDD*) of the medium at frequency ω_L. By definition of the term $\phi''(\omega)$ we could also write

$$\Delta\tau_d \cong l\left|\left(\frac{d^2\beta}{d\omega^2}\right)_{\omega_L}\right|\Delta\omega_L \tag{1.44}$$

where $\left(\frac{d^2\beta}{d\omega^2}\right)_{\omega_L}$ is the *group velocity dispersion* (or *GVD*) at frequency ω_L. Its value represents the time delay per unit length per unit pulse spectral bandwidth in the given medium [1]. If GVD is not close to zero, each frequency composing the pulse will propagate with different velocity, and this will stretch the pulse extending its time durations. For complicated structures such as a prism pair or multilayer dielectric chirped mirrors, representing the time delay in terms of GDD could be simpler.

A more detailed analysis about the impact of cavity dispersion in pulse formation, with both analytical and numerical analysis of the GDD, can be found in Ref. [21], while in Ref. [22] is given an estimation of the pulse duration taking into account all the above cited dispersion mechanics.

Third order effects

Experimentally it is demonstrated that, in order to achieve even shorter duration of the pulse, bandwidth is not the only term that takes part in the process. A pivotal role is played by TOD (*third order dispersion* term). This term is defined as

$$TOD = \phi''' = \beta''' l \tag{1.45}$$

and, taking it into account, we need to place a third order derivative in the master equation that describes mode-locking process. Both analytical and numerical solutions were discussed in Haus Moores and Nelson work [23].

1.4.2 Dispersion compensation methods

In order to get all the instrument to understand how the pulse formation process works, it's useful to give some information about the two main processes that take part in it (SPM and SAM) and the compensation methods that allow us to balance the effects of second order dispersion.

Self-phase and self-amplitude modulation: SPM and SAM

Let's take into account a Kerr medium and consider a pulse which is propagating along z-axis. After the path z, the pulse will acquire an additional phase

$$\varphi = \omega_L t - \frac{\omega_L(n_0 + n_2 I(t))}{c} z \tag{1.46}$$

where I is the intensity of the pulse and it is time dependent. The instantaneous pulse frequency will be

$$\omega = \frac{\delta(\omega_L t - \beta_L z)}{\delta t} = \omega_L - \frac{\omega_L n_2 z}{c} \frac{\delta I}{\delta t} \tag{1.47}$$

This means that the pulse frequency is dependent on the time derivative of the pulse intensity and, according to Fig. 1.12b, will evolve in time.This is the so-called *self-phase modulation* (or SPM) phenomenon. An important clarification is that, since this phenomenon induces a positive chirp, the total chirp of the pulse could be completely compensated if the medium has a negative GDD. In this case, SPM could cancel the whole effect of the pulse dispersion and let the pulse propagate without any relevant distortion. Ref. [24] will give some additional formulas about this important issue.

For what concern SAM (self-amplitude modulation) effect, we can consider a classical pulse shape. If some mechanism, like Kerr-effect or the presence of a fast saturable absorber, can introduce more losses in the tails of the pulse rather than in the central bell, this effect is called SAM. This phenomenon plays a fundamental role in pulse formation inside the resonator.

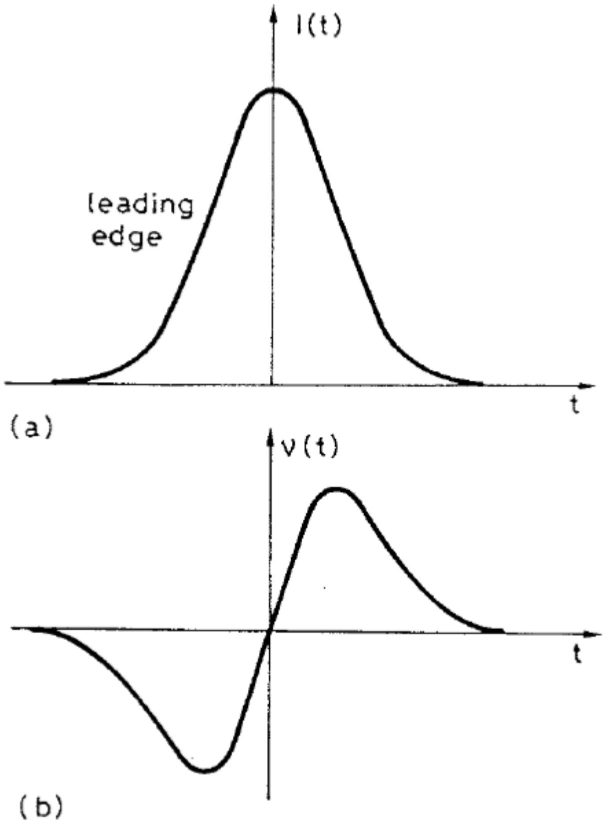

Figure 1.12: Self-phase modulation phenomenon. Time behavior of the pulse frequency, Fig. (b), when a bell-shaped pulse, Fig. (a), is traversing a medium exhibiting the optical Kerr effect. Copyright [1].

Prism compensation

In order to achieve the shortest pulse duration possible, if we neglect SPM and TOD effect, one has to put the GDD close to zero. In a typical resonator there are many elements that give a positive chirp to the laser beam, like output coupler, mirrors and the active medium it-self. For sure, all these elements give a bad influence on the dispersion and this could compromise the pulse formation.

One of the classical methods is to put four prisms in a determined sequence [26]. Referring to Fig. 1.13 we can see that the typical configuration is with the input surface of prism II parallel to the output of prism I, and the same for output of II and the input of I. Prisms III and IV have the same configuration. All the prisms are orientated so that rays propagate at Brewster angle in order to have the minimum dispersion. The angles are made such that the two pulses with frequency ω_2 and ω_1 will propagate along two different paths. The overall propagation distance for pulse at ω_1 is longer compared to the ω_2 one, and this allows to compensate the delay between the two frequencies velocity. This is

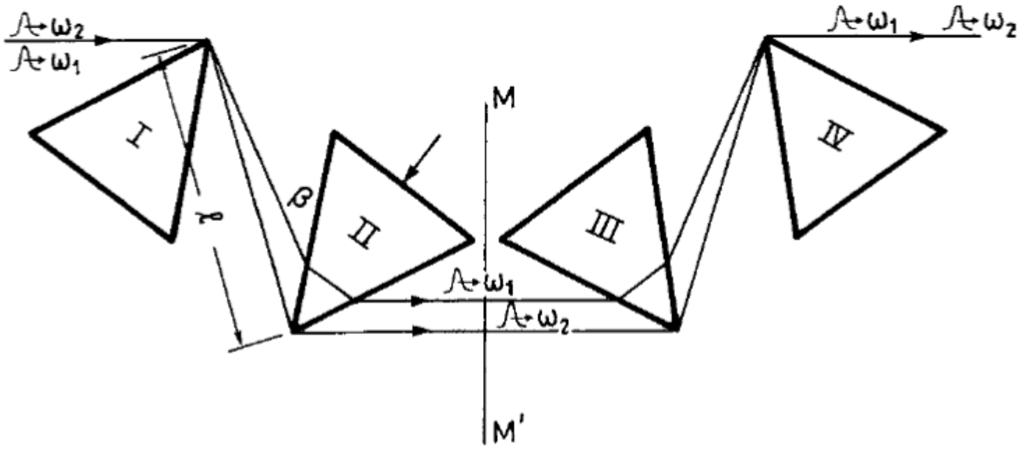

Figure 1.13: Four-prism sequence having negative dispersion. The prisms are used at minimum deviation and oriented so that the rays enter and leave at Brewster's angle. Copyright [1].

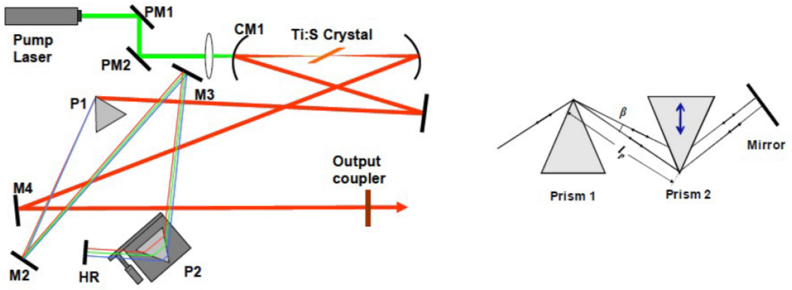

Figure 1.14: Scheme of a linear laser cavity with a prism-pair. Copyright [25].

$\tau_g(\omega_1) > \tau_g(\omega_2)$, which means a $GDD = \psi''$ less than zero.

Fig. 1.14 shows an example of laser implementation with the prism compensation methods while, on the right side, we can see the concept of the prism pair that is, from the theoretical point of view, exactly the same of the four prisms mechanism. A more detailed analysis is found in Ref. [25].

Prism-less compensation

For sure the prism compensation method is not the best solution in terms of compactness of the laser, and for this reason other methods were developed. One of the best is to use multilayer dielectric mirrors, whose detailed analysis is presented in rel [27] and [28].

In Fig. 1.15 it's possible to see an example of the optical properties of the layers: here, different materials constitute an alternated succession of higher

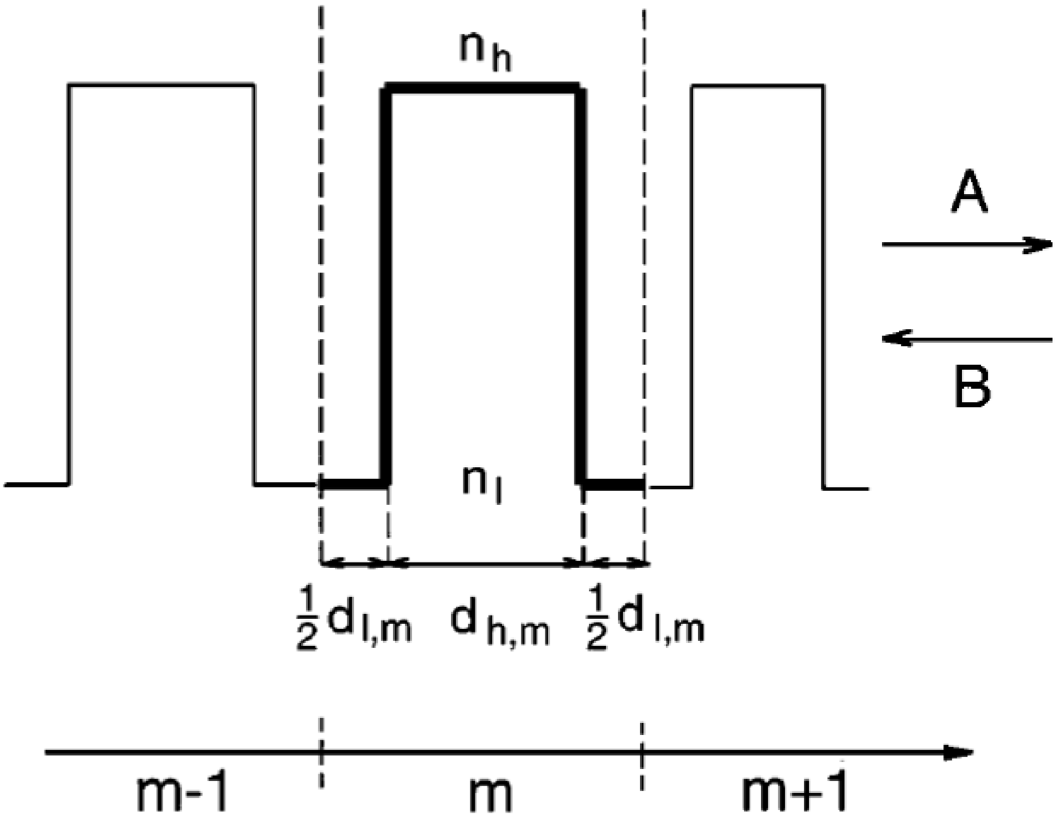

Figure 1.15: A general Bragg structure can be decomposed into a series of symmetric index steps. Copyright [27].

and lower refractive indexes. This allows to create a situation similar to the case of the prisms where different wavelength will follow different optical path, compensating normal dispersion. The single frequencies composing the pulse bandwidth, in fact, will bounce on the mirror reaching different depth and the different penetration path will take back the phase delay. Fig. 1.16 shows the composition of such mirrors.

Figure 1.16: Schematic picture of the universal structure of a double-chirped mirror. AR, anti-reflection. Copyright [27].

Chapter 2

Cr^{2+}-doped chalcogenide mid-infrared lasers

Until now mid-IR lasers are broadly demanded for their different applications in fields like sensing, spectroscopy and both industrial and medical processes (Fig. 2.1). Cr- and Fe- doped chalcogenide lasers have a large efficiency that allows output power in the order of watts with a ultra-broad emission bandwidth also operating at room-temperature: for these and other reasons, like the four-level structure, these materials are referred to as the "Ti:Sapphire of the mid-IR" [29].

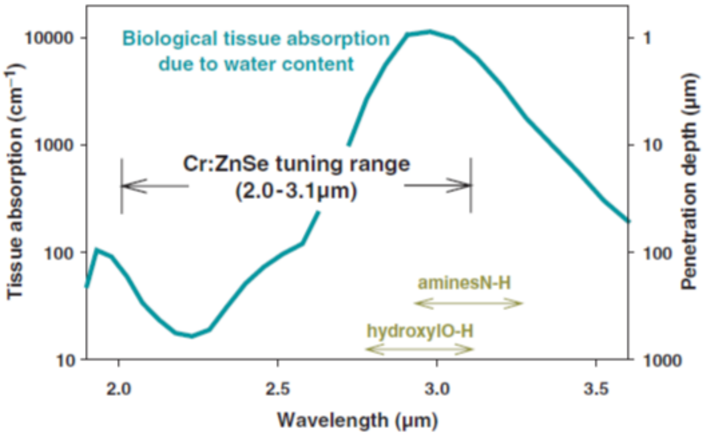

Figure 2.1: Typical absorption and penetration depth of the biological tissue, as well as the typical absorption ranges of some important radicals. Copyright [30].

In this chapter we'll analyze a particular class of host semiconductors matrix, the so called chalcogenide materials, and we will present the experimental set-up that allowed us to generate an efficient mode-locked laser based on these active media.

2.1 Solid-state lasers in the mid-IR

Referring to the bandwidth, that is one of the first requirements in ultra-short pulse generation, the F-centered (or color-centered) lasers are characterized by a broad emission bandwidth. The working principle is the use of defects energy level in impure glasses, but such lasers need a strong cryogenic and vacuum control. Fortunately, the rapid progress in the research of new materials able to operate at room temperature made these pretty-old type of lasers obsoletes. Our analysis will start, in fact, from the transition-metal and rare-heart ion doped crystalline lasers operating at room-temperature with a range between 2 and 3 μm of wavelength. This region is in facts characterized by the absorption of lots of atmospheric molecules including water (between 2.5 and 3 μm), both carbon monoxide and dioxide (2.3-2.4 μm and 2.7-2.8 μm) and nitrous oxide (2–4 μm). The ability of solid-state lasers in this region to cover in a single shot the widest wavelength possible thank to their broad-band is the main advantage of all of these kind of sources.

2.1.1 Rare-Earth and transition-metal ions doped crystals

In principle the main difference between transition-metal and rare-earth ions is, except for the wavelength, the tunability. Rare-earth like erbium or dysprosium ions do not feel any kind of perturbations depending on the host matrix where they are put. This happens because of the shield effect due to the electronic f shell (F-shield effect) inside the dopant. The transition in fact happens inside the inner shell of the element and this allows to have a fixed emission wavelength for all the various glasses type we can use as host. Differently, transition-metals like chromium or titanium, although they don't show any kind of bound with the elements of the host matrix, feel a perturbation that makes the wavelength tune depending on the different host elements (that give a different interaction). There is no shield like the previous case, and the discrete energy levels change inside the dopant. This is the case of ZnSe, ZnS and CdSe matrix doped chromium that give respectively 2.3, 2.4 and 2.6 μm of emission wavelength.

Transition-metal ions doped lasers

First tunable solid-state laser were based on 3d transition-metals, the so-called TM^{2+} ions. The two major groups are the ions that can be found in octahedral sites like Ni^{2+} or Cr^{2+} in an halides host (a binary compound where one part is an halogen atom) and those in a tetrahedral ones like Cr^{2+} (Fig. 2.2), Fe^{2+} (Fig. 2.3), Ni^{2+} and Co^{2+} (Fig. 2.2) in chalcogenides matrix. While the former are characterized by a parity forbidden electric-dipole transition (due to the presence of an inversion symmetry) that results into a low oscillator strength and long lifetime, the latter (e.g. Cr in ZnSe) present an high oscillator strength, a shorter lifetime and a lower field splitting that allows transitions shifted more into infrared.

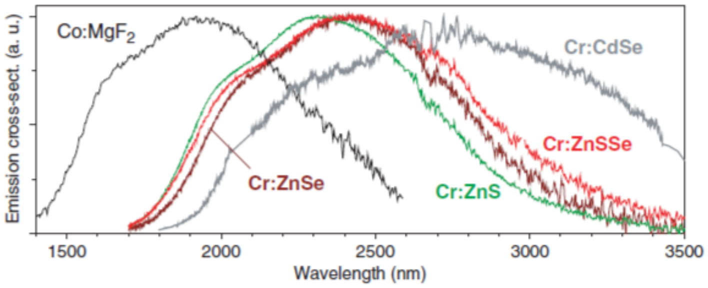

Figure 2.2: Gain curves of some the existing ultra-broadband mid-infrared lasers at room temperature. Copyright [30].

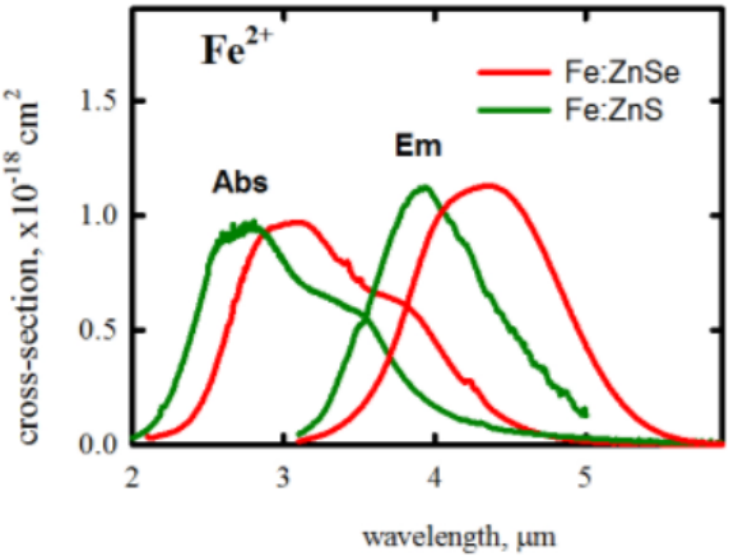

Figure 2.3: Gain curves of Fe- doped chalcogenide laser at room temperature.

Broadband solid-state lasers based on transition-metals are a simple and an efficient alternative to more complex and costly semiconductor lasers in the mid-infrared, thank to their wide tunability (that can reach $0.5\lambda_0$) and the possibility to generate few cycles optical pulses. Thank to the early research in the field of mid-infrared sources, now chromium based lasers are perfectly comparable in power and performances to the Ti:Sapphire ones, giving the opportunity to have a stable and efficient CW or pulsed laser in the infrared. One of the first ultra-band laser has been the $Co^{2+} : MgF_2$, whose tunability extends between 1.75 and 2.16 μm, but the necessity of cryogenic cooling stopped its development in the industrial and commercial field. The invention of a new class of transition-metal doped zinc chalcogenides, occurred in the middle af nineties, gave the possibility to propose similar families of chromium doped cadmium chalcogenides like CdSe and CdTe and, in the end, ZnSe, ZnS and ZnTe. All of these crystals present their ions placed in tetrahedral sites. The lower maximum phonon frequency, that allows a decrease of the non-radiative decay rate and an increase of the fluorescence quantum efficiency, belongs to $Cr^{2+} : ZnSe$ [30].

Rare-earth ions doped lasers

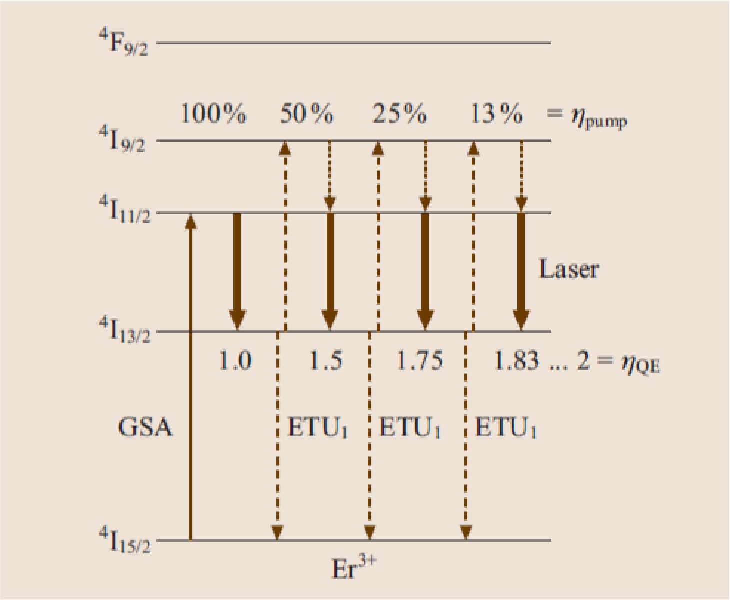

Figure 2.4: Partial energy-level scheme of erbium illustrating the process of energy recycling from the lower to the upper laser level by ETU. Indicated are the relative pump rate ν_p of the upper laser level and the quantum efficiency ν_{QE} which increases from 1 to 2 if a large number of ions participate in the process. Copyright [45].

The main issue that characterize rare-earth doped crystals in rare-earth based lasers and that makes these kind of sources so attractive is their strong sharp-line fluorescence. The interaction of the 4f electrons with the crystal field allows that the most of the degeneracy in the single ion energy levels are removed by the Stark effect and this determines the impurities energy levels that, interacting dynamically with the lattice phonons, are responsible for the particularly narrow line-width and internal efficiency. All the rare-earth lasers have a 4-level structure where the terminal state of the transition is a crystal-field split or a spin-orbit component of the ground state, depending on the particular ion taken into account. One of the most important mid-infrared solid state laser is the

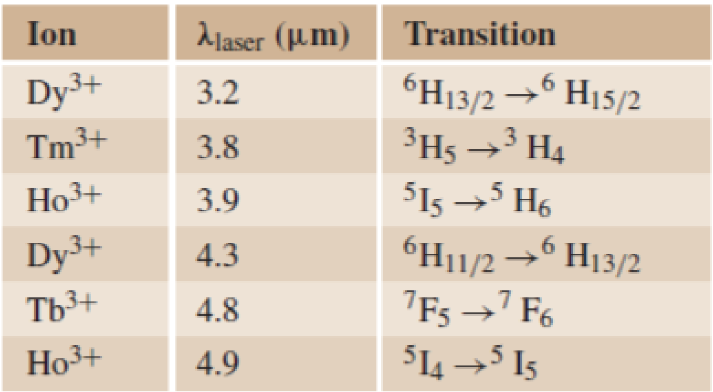

Ion	λ_{laser} (μm)	Transition
Dy^{3+}	3.2	$^6H_{13/2} \rightarrow ^6 H_{15/2}$
Tm^{3+}	3.8	$^3H_5 \rightarrow ^3 H_4$
Ho^{3+}	3.9	$^5I_5 \rightarrow ^5 H_6$
Dy^{3+}	4.3	$^6H_{11/2} \rightarrow ^6 H_{13/2}$
Tb^{3+}	4.8	$^7F_5 \rightarrow ^7 F_6$
Ho^{3+}	4.9	$^5I_4 \rightarrow ^5 I_5$

Figure 2.5: Examples of luminescent transitions investigated as candidates for mid-infrared lasers in sulfide glasses. Copyright [45].

erbium doped one (that usually emits around 2.7 μm), whose inner transitions are shown in Fig. 2.4. Usually the requirements for a CW laser operating at room temperature are:

- level two unpopulated at room temperature (energy greater than K_bT)
- large line gap between level two and level three
- prevalent radiative relaxation for level three
- lifetime of level two shorter than lever three
- high population of level four

Closed 5p shell screens the inner electrons of the ion, and for this reason the interaction tensor operator ($U^{(t)}$) doesn't change significantly if we change the host material. This involves that, if we want to calculate the transition probability, we are allowed to use, for all the different combination af hosts, the same matrix elements computed for the free ion. Nevertheless, we have also to take into account that the intensity parameter (Ω_t) is quite sensitive to the crystal symmetry and can vary up to five times depending on the host. Therefore, the best solution that has been found is to have the same value of t for both $U^{(t)}$ and Ω_t: this will lead to an optimum for the stimulated emission cross-section.

In order to give an example of the typical values of this solid-state laser based on rare-earth doped crystals, we present some of the most relevant data (like emission wavelength and transitions) Tb^{3+}, Dy^{3+}, Ho^{3+} and Tm^{3+}.

2.1.2 Semiconductor lasers

This subsection will give an idea of the different semiconductor lasers that can be built with a chalcogenide matrix. We will focus on lead salt and indium antimonide lasers.

Lead salt diode lasers

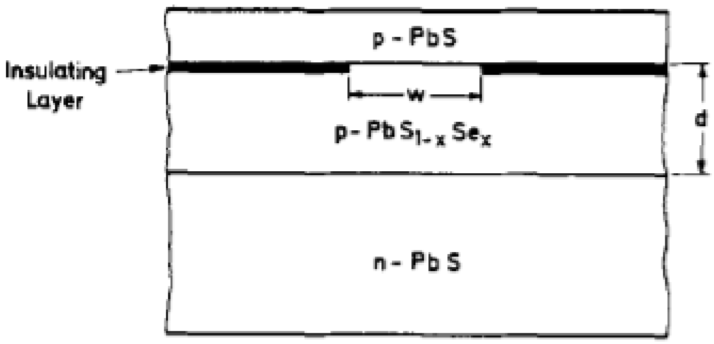

Figure 2.6: Double hetero-junction structure for lead salts laser. Copyright [32].

The small energy gap ($\Delta E \approx 0.3eV$) belonging to lead chalcogenides has driven this direct semiconductors to the top of the list in the useful material for opto-electronic devices. Laser diodes based on these particular materials have a large emitting range between 2 and 20 μm and are characterized by a low threshold current density and high temperature operation. Type of lead salt semiconductors are $Pb_{1-x}Sn_xTe$ and $PbS_{1-x}Se_x$. PbS, PbSe and PbTe crystallize in the same way of SnTe in a cubic NaCl structure [32] and they have almost the same lattice constant. Solid solubility is obtained for $Pb_{1-x}Sn_xTe$ and $PbS_{1-x}Se_x$ while $PbS - SnS$ and $PbSe - SnSe$ do not exhibit this property because of their orthorhombic structure. Staying in the solid solubility range, another important issue is that PbTe-SnTe shows a ΔE close to zero for a certain composition x_c, and this is actualized in a change of several alloy's physical properties: the band-gap increases with the temperature for PbS, PbSe and PbTe but not for SnTe and decreases with a progressive hydrostatic pressure increment for PbS, PbSe and PbTe but not for SnTe. Moreover, PbS, PbSe and PbTe enlarge their band-gap in presence of a strong magnetic field. All these physical mechanisms allow laser sources based on these materials to be tuned in wavelength by temperature, pressure or H-field.

In order to have stimulated emission end laser action, a larger difference between the quasi-Fermi levels than the band-gap is needed. One of the most important figure of merit of this kind of lasers is the threshold current density

(J_{th}) that is directly proportional to the active region thickness (d) and indirectly proportional to η_i, the quantum efficiency. In lead salts d results to be in the order of 20 μm for an homo-junction structure while for a symmetrical junction where carrier number density of minority charges is equal to the majority one (n=p) the thickness result to be the double. It has been demonstrated that operation at room temperature is possible for $\lambda = 2 - 6.2 \mu m$, but for wavelength close to the lower limit needs still to be achieved a low J_{th}. The highest mid-infrared diode laser operation temperature observed is reported in Ref [33], where a $PbSrSe$ heterostructure is demonstrated to achieve laser action up to 60 Celsius degrees. In Fig. 2.6 we can see the usually adopted hetero-junction structure.

The small line width of this kind of lasers allows to use them for ultra fine gas spectroscopy. Many gases like NH_3, C_2H_2, CO, SO_2, NO and H_2O were analyzed by tuned lead salts diode lasers. In Fig. 2.7 it's possible to see a typical line width.

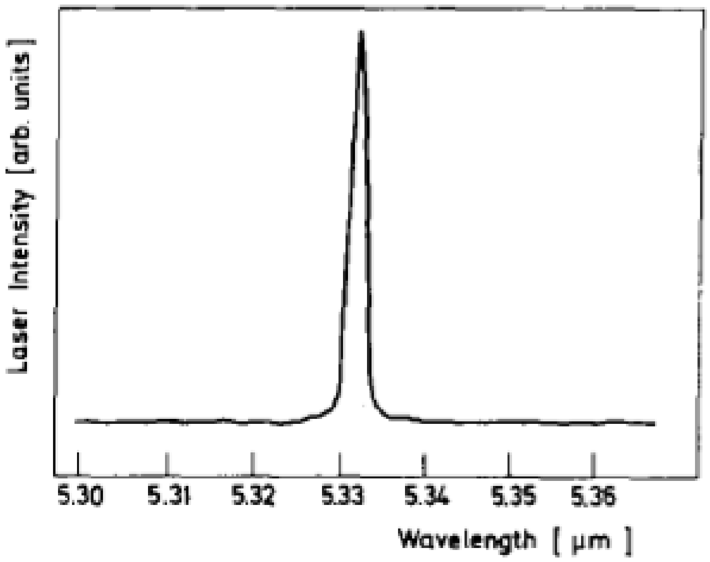

Figure 2.7: Typical wavelength and line width of a $PbS_{1-x}Se_x$ homo-junction laser. Copyright [32].

Indium antimonide solid-state lasers

When we talk about antimonides we are referring to that elements belonging to group III-V of the semiconductor family and all these materials can be grown on a substrate of GaSb or InAs. In the photonic devices market all the materials belonging to this family (GaSb, InAs, AlSb, InSb) are very attractive thanks to their both electrical and optical properties that allow to cover a wide spectral range in the mid-IR. The allowed spectral range chances between 0.15 eV to 2 eV and also the difference in the conduction energy between different materials can go up to 2 eV: this means an extended combination possibility, made it possible thanks also to the different types of band alignment we can built in antimonide hetero-structures. Lasers based on this type of materials have been, and still now, used to emit above $2\mu m$, operating at room temperature. Quantum-well for the type-II structure is also possible in order to reduce the Auger recombination and to increase emission wavelength. Inter-band cascade lasers that use a succession of II and III type are demonstrated to reach $6\mu m$ wavelength at room temperature and up to $11\mu m$ at lower temperature in a pulsed regime. Quantum Cascade Lasers (QCLs) based on InAs/AlSb can operate at $21\mu m$ and this is very promising in order to develop THz QCLs. Progresses in the photo-detector and electronic devices technology based on III-V group are reviewed in [34] and [35].

2.2 Cr^{2+}-doped chalcogenide crystals

As we just mentioned in the first section, transition metal doped chalcogenide are one of the most important crystals allowing efficient emission in the mid-IR. In particular, the Cr^{2+} ions filling tetrahedral sites are known for their high quantum efficiency and luminescence between 2 and 3 μm. This section will analyze Cr^{2+}-doped chalcogenide crystals properties in order of advantages, efficiency and tunability, focusing on the two of them we used for our set-up: $Cr^{2+}:ZnSe$ and $Cr^{2+}:ZnS$.

2.2.1 Chalcogenide class

The presently available mid-infrared sources like lead-salt diode or rare-heart solid-state lasers present large efficiency and, in some case, tunability, but in order to have a good stability they may require an injection-seeding with at least one shorter wavelength. For this reasons, a new class of transition-metal ions doped chalcogenide is required, and this is the case of $Cr^{2+}:ZnSe$ and $Cr^{2+}:ZnS$, whose high slope efficiency give the chance to apply them easily in different fields of the research. Cr, Co, Ni and Fe are candidates to emit in IR region and present good properties in terms of absorption, cross-sections, emission lifetimes and emission quantum yields [36]. A review of the full set of transition-metal dopants can be found in Ref. [37]. Transition-metal ions belonging to II-IV groups are known for their tendency to crystallize in a tetrahedrically way, which allows a smaller splitting of the crystal-field compared to the octahedral coordination and, consequently, a more shifted wavelength into IR. Moreover, the non-centrosymmetric component of the crystal field, that is completely absent in an octahedral symmetry, enhance the 3d-4p configuration mixing, increasing the radiative transition rate and, consequently, the quantum yield. Structures as ZnS, ZnSe, CdS and CdSe will give a smooth change in the dopant ion energy level, and this explains why chromium, if put into a different chalcogenide matrix, can tune its emission wavelength between 1.9 and 3.3 μm [38]. Kerr-lens mode-locking has been recently demonstrated and improved for ZnSe and ZnS, reaching 2 W output average power, 24 nJ pulse energy and less than 29 fs pulse duration, giving an appealing alternative to the inefficient ultra-fast mid-Ir sources like OPOs, OPAs and DFG based ones.

2.2.2 Optical properties and emission efficiency

Zinc-blende semiconductors have a pretty high second-order nonlinear susceptibility (16 and 4 pm/V for ZnSe and ZnS respectively). $Cr^{2+}:ZnS$ and $Cr^{2+}:ZnSe$ structures consist of microscopic single-crystal grains and the broad distribution of grains orientations give a linear dependence of the conversion yield with the medium length and a wide bandwidth, as property of random quasi-phase-matching condition. Another interesting property is the high third-order non-linearity of both these crystals. The non-linear refractive index n_2 of ZnSe and ZnS are more than 50 times larger than CaF_2 one and the critical power of self-focusing is quite accessible (400 kW in bulk for a 2.4 μm input wavelength). ZnSe has just been discovered to show a spectral broadening of 450 nm with a pump laser of 2 μm and also a 3-octave-spanning super-continuum has been created. Therefore, we can say that the combination of both second and third non-linearities and the particularly promising ultra-fast laser capabilities of these two crystals give a great number of possibilities. The random quasi-phase-matching in $Cr_{2+}:ZnS$ and $Cr_{2+}:ZnSe$ media makes arise an efficient SHG directly in the gain element of KLM laser and, in rare cases, also three wave mixing effects like third and even fourth harmonic generation. DFG and OPOs methods can be also used to reach beyond 3 μm wavelength.

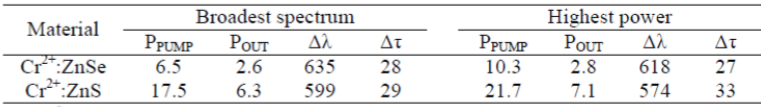

Material	Broadest spectrum				Highest power			
	P_{PUMP}	P_{OUT}	$\Delta\lambda$	$\Delta\tau$	P_{PUMP}	P_{OUT}	$\Delta\lambda$	$\Delta\tau$
Cr^{2+}:ZnSe	6.5	2.6	635	28	10.3	2.8	618	27
Cr^{2+}:ZnS	17.5	6.3	599	29	21.7	7.1	574	33

Figure 2.8: P_{PUMP} (W), P_{OUT} (W), $\Delta\lambda$ (nm), $\Delta\tau$ (fs). Copyright [38].

Few examples of the recently achieved performances for ZnSe and ZnS are shown in Fig. 2.8.

In order to study the energy levels, the Hamiltonian for non-interacting defects in a host matrix can be written as

$$H = H_F + H_{CF} + H_{JT} + H_{SO} + H_{SS} + H_B \tag{2.1}$$

where the first term is the free-ion term without spin effects, the second takes into account the interaction of the crystal with the electric field, the third causes the Jahn-Teller distortion, the fourth is the spin-spin coupling and the last one represents the effect of the magnetic field [39]. Typically, for ions belonging to II-VI groups, the term H_{CF} is smaller than H_F but bigger than H_{SO} and H_{SS}. Neglecting H_{JT} in first approximation, we can say that the Cr^{2+} free-ion ground state is ^5D. A crystal field H_{CF} of a tetrahedral symmetry T_d will split this ground state by Δ (C-F-splitting) into ^5E (orbital doublet) and $^5T_2$ (orbital triplet) where the last one will be the new ground state for chromium ion.

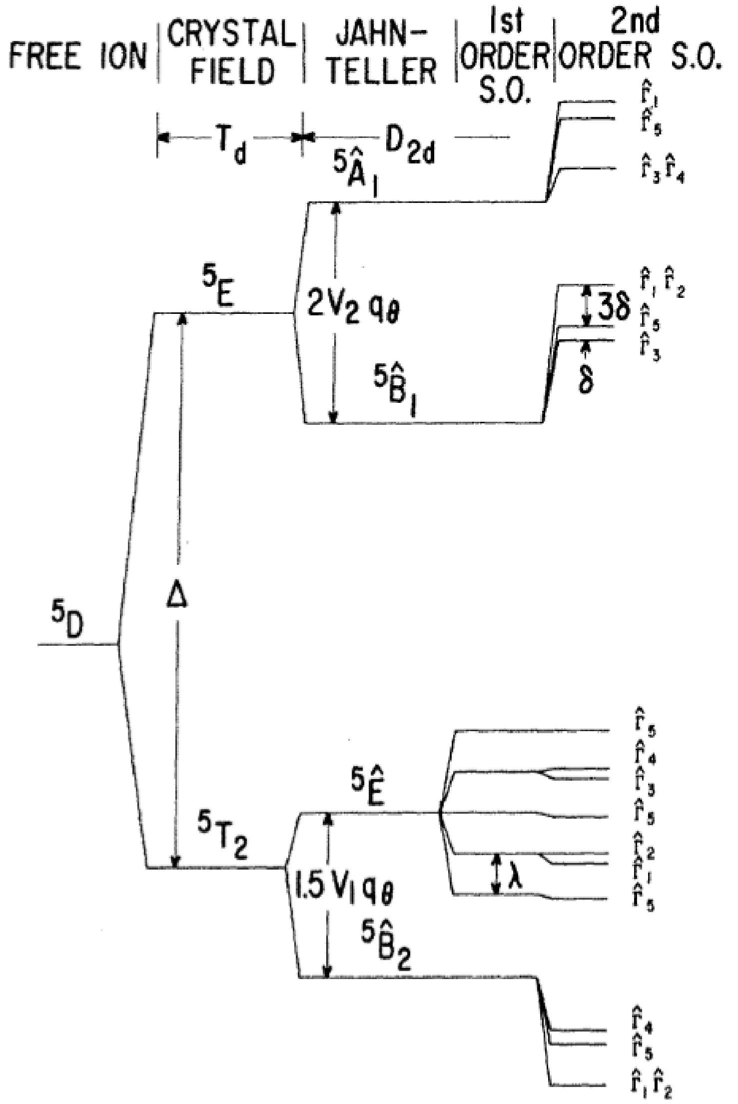

Figure 2.9: Energy levels og Cr^{2+}. Ground state is $\Gamma_1\Gamma_2$ of $^5B_2$. Copyright [39].

Another further splitting will be made by considering Jahn-Teller, spin-orbit and spin-spin coupling. Fig. 2.9 shows this splitting process. Different models (emitting at different wavelength) for the chromium are possible, and Fig. 2.10 give an example of the possible transition used for laser action in the infrared region in a chromium doped ZnSe. Usually, for a tetrahedrally coordinated Cr^{2+}, the transition $^5T_2 \rightarrow ^5 E$ is typically observed and its maximum is around 1.7-1.9 μm.

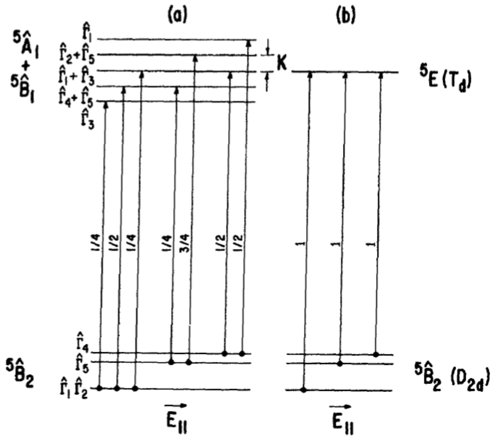

Figure 2.10: Allowed electric dipole optical transitions of Cr^{2+} in ZnSe for the infrared model: (a) when $K(^5E)$ splitting of ^5E orbital state is observable; (b) when $K(^5E)$ is too small to be resolved experimentally. Copyright [39].

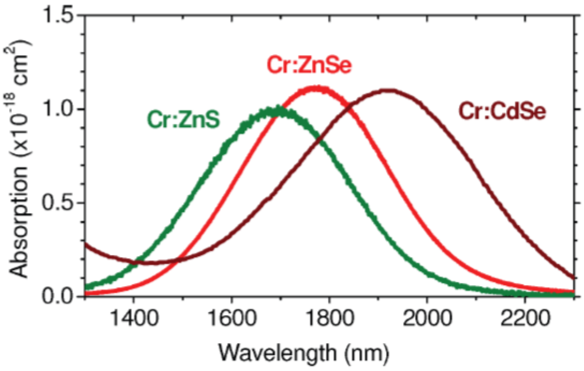

Figure 2.11: Optical absorption coefficient vs wavelength for three different Cr-doped crystals. Copyright [30].

In Fig. 2.11 it's possible to appreciate graphically the different shift in the energy levels due to the change of the host. CdTe, CdS, ZnSe and ZnS absorption spectra are analyzed and the wavelength shift in the absorption transition is quite broad, covering a spectrum between $\sim 1,6\mu m$ for the ZnS ($6000 cm^{-1}$) to $\sim 2\mu m$ for the $CdTe$ ($5000 cm^{-1}$).

The emission occurs between 2 and 3 μm (Fig. 2.12) and both the absorption and emission cross-section are in the order of $\sim 10^{-18} cm^2$, as expected for a Cr^{2+}-doped chalcogenide with a tetrahedrally coordination.

This kind of materials have usually an high thermal conductivity but not in the case of CdSe. This is the cause behind the strong thermal lens effect of this

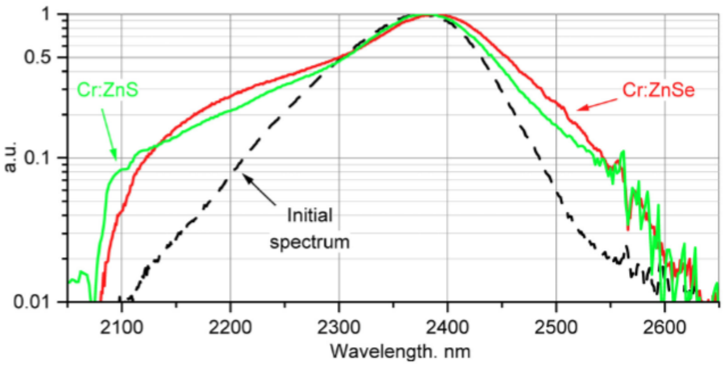

Figure 2.12: Room temperature emission spectra of Cr^{2+}-doped chalcogenides. Copyright [38].

Host material	**ZnS**	**ZnSe**
Transparency (μm)	0.4 - 14	0.5 - 20
n at $3\mu m$	2.26	2.44
GVD at peak (fs^2/mm)	123	218
n_2 at $1.06\mu m$ ($\cdot 10^{-20} m^2/W$)	84	460
$[1/n][dn/dT]$ ($\cdot 10^{-5} K^{-1}$)	1.9	2.6
Thermal conductivity (W/cmK)	0.27	0.19
σ_{abs} ($\cdot 10^{-20} cm^2$) at $1550\mu m$	~80	~50
σ_{em} ($\cdot 10^{-20} cm^2$)	75	90
τ_{em} ($300K$) (μs)	8	9
Dimensions (mm)	2.0 x 6.9 x 7.2	2.8 x 4.9 x 5.0 uncoated
N_{Cr} ($\cdot 10^{18} cm^{-3}$)	8.0	9.2
I_{abs}/I_0	72.2%	72.4%

Table 2.1: Thermal and optical values for ZnS and ZnSe crystals.

crystal. Has we already said, chalcogenides show a large second and third order effects, giving the possibility to use the kerr-effect for the soft-aperture mode-locking. In Tab 2.1 are presented the values of GVD, thermal conductivity, linear and non-linear refractive indexes, dimension and Cr^{2+}-doping level of the crystals we used for the experimental set-up.

For the absorbed power estimation we used Lambert-Beer law in this formulation

$$\frac{I_{abs}}{I_0} = \frac{I_0 - I_{LB}}{I_0} = 1 - e^{-\alpha_0 L} = 1 - e^{-N_{Cr}\sigma_{abs} L} \tag{2.2}$$

where N_{Cr} is the dopant concentration, σ_{abs} is the absorption cross-section and L is the dimension of the crystal in cm.

Fig. 2.13 represents an example of the group velocity dispersion characteristic for wavelengths from 2 to 3 μm passing trough a ZnSe crystal.

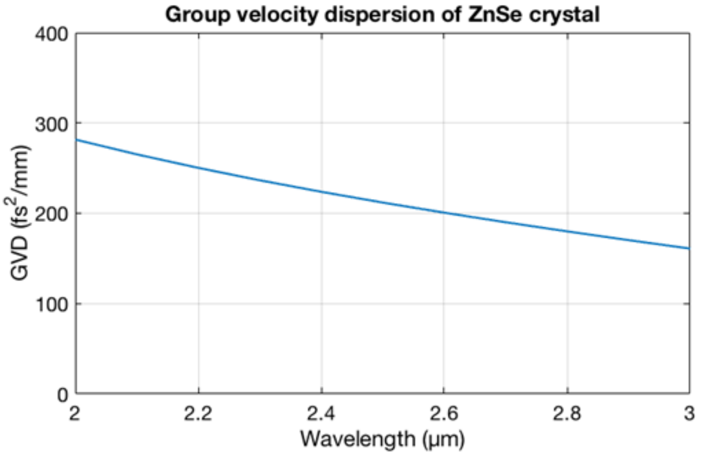

Figure 2.13: Group velocity dispersion in ZnSe.

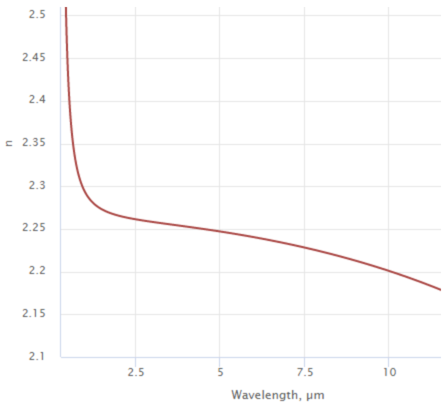

Figure 2.14: Refractive index for ZnS crystal.

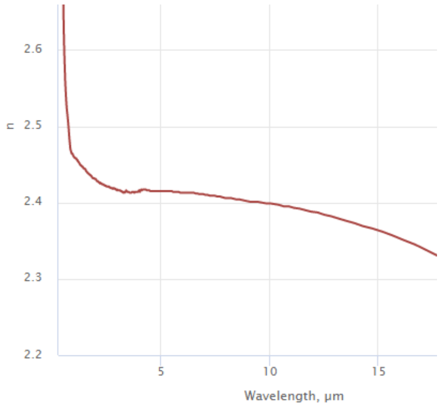

Figure 2.15: Refractive index for ZnSe crystal.

Fig. 2.14 and 2.15 show the non-linear wavelength dependence of the refractive index for ZnS and ZnSe cases.

2.3 Experimental set-up

This section will explain our experimental configuration for the realization of an efficient $Cr^{2+} : ZnSe$ and $Cr^{2+} : ZnS$ laser. Here below are presented the technical parameters and the practical arrangements.

2.3.1 Pumping system

For what concern the pumping system, we used a commercial Erbium fiber laser (ELM-20-LP). This laser emits up to 20W linearly polarized CW output beam at the emission wavelength of $1.57\mu m$ and its line-width $\Delta\lambda \sim 0.4 - 1.0nm$. The beam size (diameter) at output, measured at $1/e^2$ of the intensity, is $W_p \sim 4mm$ with a divergence angle of $\theta_{div} \sim 0.6 - 1.0rad$ and an M^2 factor of 1.05. In Fig. 2.16 it's easy to appreciate the output spectrum and the line-width of this commercial laser.

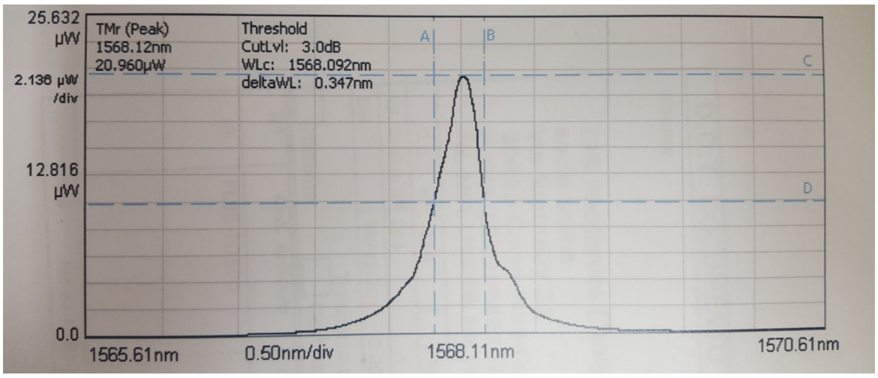

Figure 2.16: Laser output spectrum at nominal output power.

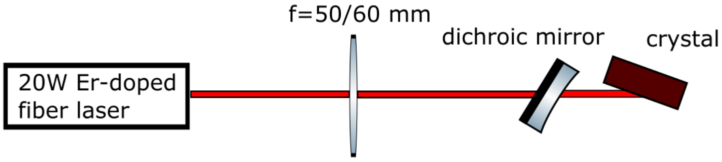

Figure 2.17: Pump system.

In order to exploit in an efficient way the infra-red transition in chromium-doped crystals a more focused beam into the active media is needed. For this reason it has adopted a focusing lens between the pump laser and the active region. Fig. 2.17 represents this configuration. Different plano-convex lenses have been used. The best results have been reached with the 60 mm and 50 mm focal length plano-convex lenses. Between the crystal and the lens a dichroic mirror has to be put in order to complete the 6 mirrors cavity. Using LASCAD

Pump value (mV)	Input beam (mW)
281	220
385	636
480	1130
580	1660
680	2210
780	2700
880	3200
980	3620
1080	4150
1180	4670
1280	5300

Table 2.2: Power input at crystal surface (mW) vs technical parameter (mV) of the pump laser.

we simulated the beam focusing inside the crystal: the estimated result is $W_0 \sim 20\mu m$ of beam diameter. Tab. 2.2 and Fig. 2.18 shows power input at crystal surface compared to the voltage value of the pump. All the further plots will refer to the input power at crystal surface taking into account this conversion.

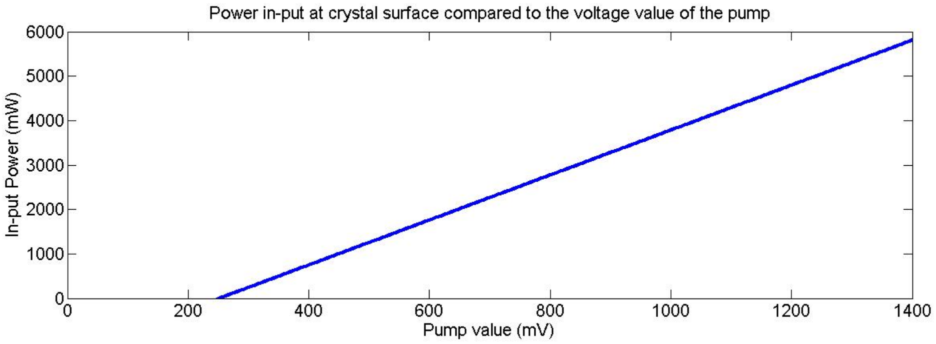

Figure 2.18: Power input at crystal surface (mW) vs technical parameter (mV) of the pump laser.

2.3.2 Laser cavity configuration

Our configuration (Fig. 2.19) is composed by a 6 mirrors asymmetric x-folded linear cavity. The first two ones around the crystal are curved chirped mirrors with a 50 mm radius of curvature. The three others on the left arm of the cavity are plane but with the same characteristics of the previous ones (high reflective for 2.3-2.6 μm and a dispersion compensation of $\sim 200 fs^2$). As we told before, we used both 50 and 60 mm focal lenses and we tried also different transmissive output coupler (1 and 3 percent).

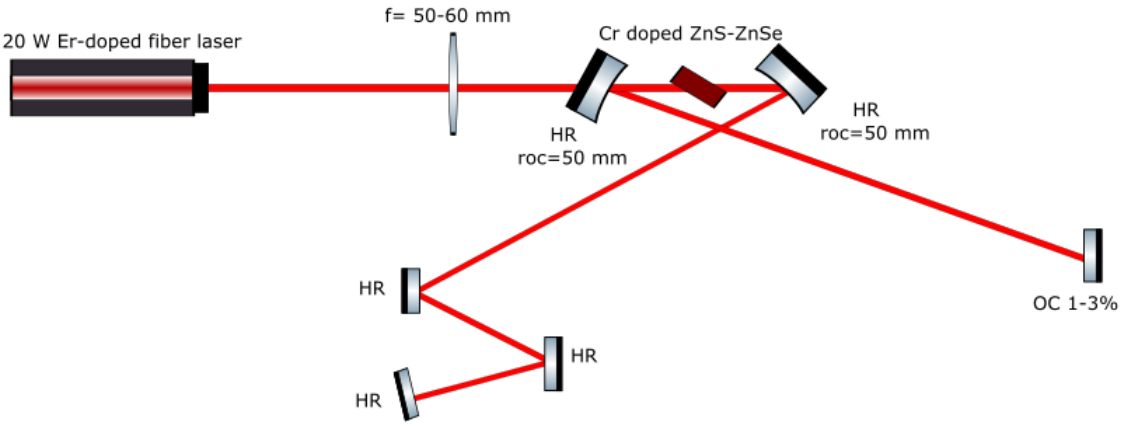

Figure 2.19: Set-up configuration for both 150 and 250 MHz cavity.

By changing cavity arms length we can get different repetition rate for a pulsed regime, and we focused on two particular cases: 150 MHz and 250 MHz. According to $f_{rep} = c/2L$, that holds for a linear cavity configuration, the corresponding length value for the two cases are 1 m for 150 MHz and 0.6 for 250 MHz.

Crystal is always set to Brewster angle that is 67° or 69° for ZnS or ZnSe, respectively. Changing the relative distance between the curved mirrors we can also analyze the stability region of our configuration. As it's possible to see in Fig. 2.20, the stability region is actually split into two sub-regions. This is because of the asymmetry in the cavity configuration that inevitably reflects into an asymmetry in the propagation matrix.

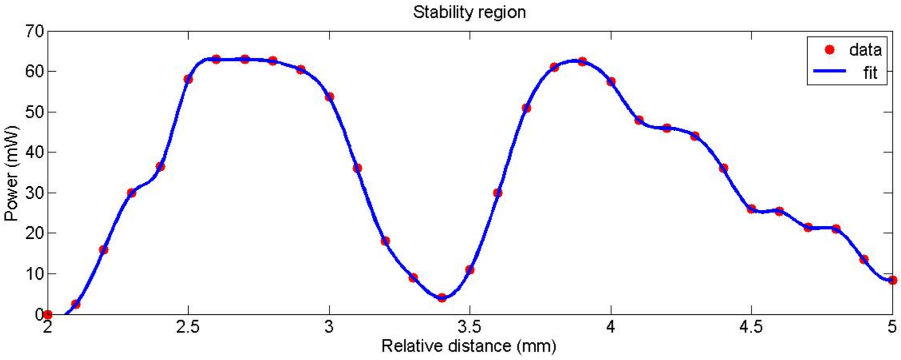

Figure 2.20: Output laser power versus relative distance between curved mirrors around the crystal for a 250 MHz repetition rate $Cr^{2+}ZnS$ laser with 1 percent output coupler.

2.3.3 Temperature control and nitrogen purging

Temperature control and nitrogen purging have been also important in order to achieve the best performance. Our technical choices are described here below.

Temperature control

Figure 2.21: Peltier device.

A good crystal temperature control is needed in order to manage and reduce thermal effects. For this reason we operated putting, first of all, a Peltier device just between the downer crystal surface and the metallic support. This kind of thermoelectric cooling uses, in facts, the Peltier effect to create a heat flux between the junction of these two materials, managing their temperature. The structure is constitute by a sequence of n-type and p-type semiconductors, as shown in Fig. 2.22, in order to be thermally in parallel but electrically in series. A voltage difference applied to the surface will induce a DC current flow that will drive the heat flux in a determined direction, depending on the voltage sign value.

Another important expedient is to use a water cooling system in order to reduce the temperature of the metal directly in contact with the crystal. Using both this techniques together allow a fine control of the crystal temperature, ensuring the higher efficiency.

Using both these techniques together we managed to fix the crystal temperature around 20°C.

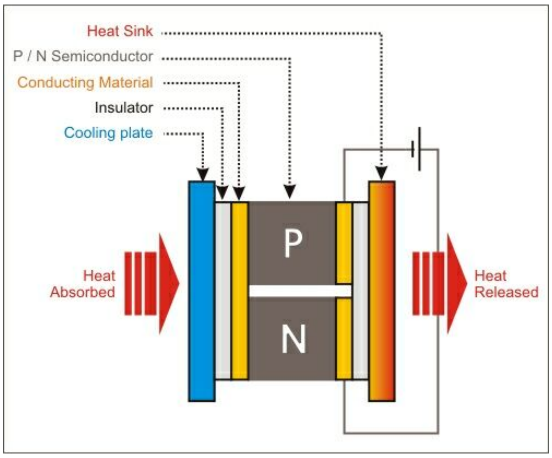

Figure 2.22: Peltier device structure: heat flux is driven from the left to the right thanks to current flowing between the semiconductor junction.

Nitrogen purging

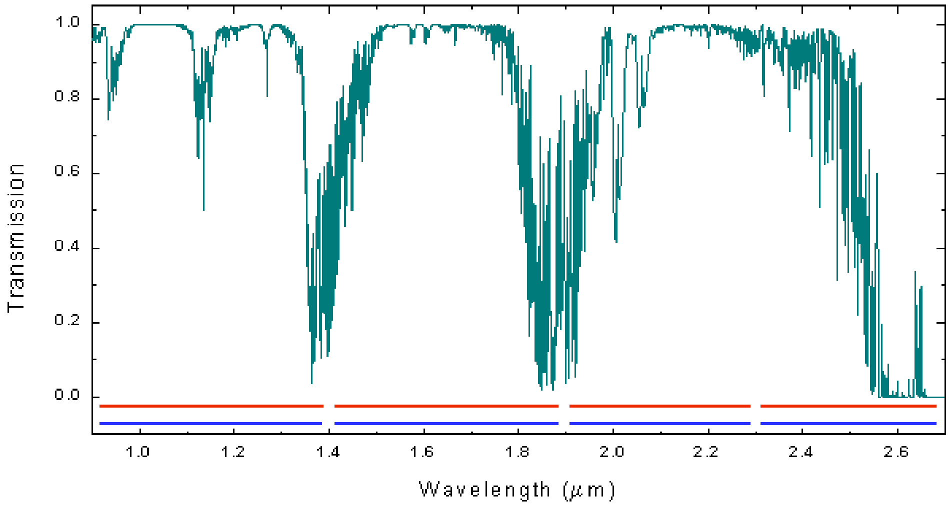

Figure 2.23: Atmosphere transmission in the mid-infrared for 1m propagation length.

Due to the particular output laser wavelength we were operating at, the choice of nitrogen purging has been made. Atmosphere, in fact, is composed by many molecules (like water) that have a peak in the absorption at exactly our output wavelength region (2.3-2.4 μm). For this reason nitrogen has been essential in order to reduce intra-cavity losses and get the highest bandwidth in mode-locking regime.

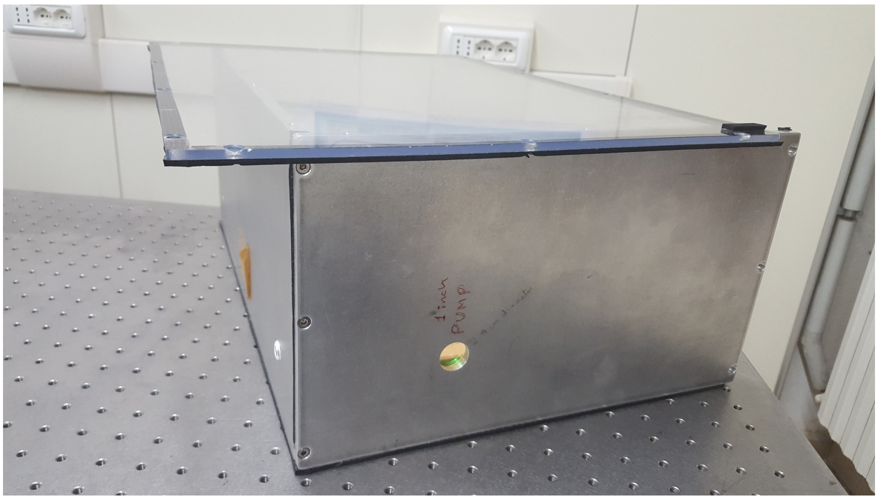

Figure 2.24: Non-hermetic box used to maintain the laser under nitrogen purging.

As shown in Fig. 2.23, in 2-2.6 μm region atmosphere doesn't present a big absorption peak, but all the spectral narrow absorption lines induce leaks that, albeit not excessively high, could limit mode-locking bandwidth and affect, consequently, performances. Since working in vacuum condition could have been hard and also not really necessary, we used a non-hermetic box (Fig. 2.24) where nitrogen can be driven inside it by a rubber tube.

2.3.4 Prism-less dispersion compensation

GVD compensation is absolutely necessary to get the mode-locking regime, and a fine compensation of the same allows to reach the theoretical limit for the pulse duration. As explained in Chapter 1 different methods are currently available, but for a compact cavity like ours the best choice should be to minimize optical elements inside it. For this, prism-less solution are preferred over unpractical ones like prisms sequences. Chirped mirrors allow to compensate a quite good amount of dispersion for each bounce, introducing a delay opposite respect to the common different wavelength velocity.

Our chirped mirrors GDD characteristic (Fig. 2.25) makes evidence of the negative dispersion introduced for each bounce that is, for our wavelength, around $200 \sim 250 fs^2$. We can also evaluate the third order contribution estimating the plot slope around our center wavelength. Around 2400 we have $\frac{-200}{200}\frac{fs^2}{nm} = -1\frac{fs^2}{nm}$. Anyway, as we already said, we neglected third order contribution in our work.

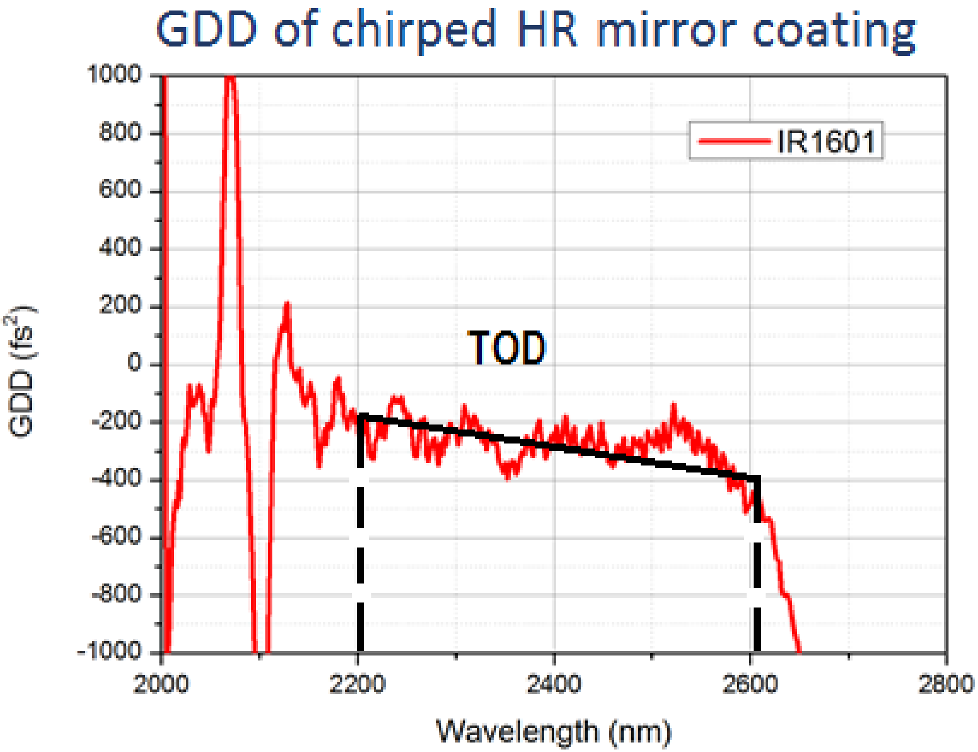

Figure 2.25: GDD of chirped HR mirror.

Tab. 2.3 gives the explicit values estimated for all the elements that take part in group delay dispersion process. According to our configuration, 5 chirped mirrors in a linear cavity means 9 bounces, and this gives a compensation of -1800 fs^2. The double-pass trough the crystal gives +680 x 2 = +1360fs^2 and, taking into account also air and output power dispersion, we get -370 fs^2 of net round-trip GDD. Negative values close to zero for the total GDD is the starting point for a stable mode-locking regime. For what concern ZnS crystal we used only 3 chirped mirrors in a 6 mirrors laser configuration in order to better compensate the smaller GDD value of the crystal compared to the ZnSe one.

	Cr^{2+}:ZnS (2.30 mm)	**Cr^{2+}:ZnSe (3.04 mm)**
Components	**GDD(fs^2)**	**GDD(fs^2)**
Chirped mirrors	-200 x 5 (bounces)	-200 x 9 (bounces)
Output coupler	+50	+50
Air (2.1 m)	+20	+20
crystal	+250 x 2 (double pass)	+680 x 2 (double pass)
Round-trip net GDD	-430	-370

Table 2.3: GDD values for different optical elements.

Chapter 3

Characterization of mode-locked Cr^{2+}:ZnSe and Cr^{2+}:ZnS lasers

This chapter will give all the experimental results about $Cr^{2+} : ZnS$ and $Cr^{2+} : ZnSe$ lasers, focusing on 150 MHz and 250 MHz configurations with 3% output coupler and, for some case, also 1% output coupler. All measurements are referring to the cavity configuration presented in Fig. 2.19 with 50 mm focal lens. Total cavity length will change according to the repetition rate: 1 m for 150 MHz and 0.6 m for 250 MHz.

3.1 Output power characteristic

Output power is an interesting characteristics to analyze and now we will present the efficiency conversion between input and output power, giving an idea of the slope efficiencies typically involved for these kind of crystals depending on the output coupler transmission.

3.1.1 Continuous wave configuration

Tab. 3.1 and Fig. 3.1 refer to ZnS host crystal. It's possible to appreciate the comparison between 1% and 3% output coupler. As shown in Fig. 3.1 the slope efficiency is much higher for 3% output coupler, as we would have expected since the other one has a lower transmission coefficient. According to Tab. 3.1, slope efficiency for 1% is 3.6% while for 3% output coupler is three times that value (10.7%). Intra-cavity power is comparable in both cases (∼12 W for an incident power equal to 2.8 W).

Tab. 3.2 and Fig. 3.2 show the same characteristics for ZnSe. Here has been decided to take the measurement only for the 3% output coupler that allowed us to reach higher power. This measurements have been taken optimizing a little bit the set-up for the continuous wave, and for this main reason, as well as for

CW output power vs incident power for ZnS with both 1 and 3 percent output coupler

Pump (W)	**1 % O.C. (mW)**	**3 % O.C. (mW)**
0.77	34	83
1.47	72	187
2.1	90	260
2.8	120	330
3.5	190	400

Table 3.1: CW output power vs incident power for ZnS with both 1 and 3 percent output coupler.

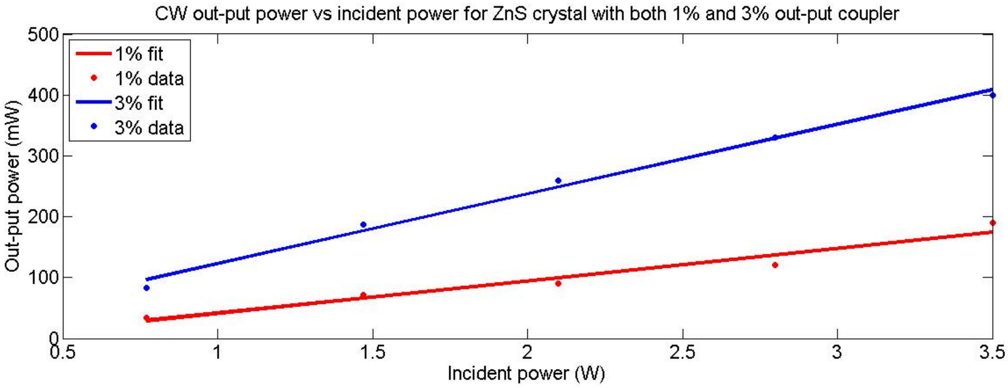

Figure 3.1: CW output power vs incident power for ZnS with both 1 and 3 percent output coupler.

the fact that ZnSe has a different absorption cross-section and we used a longer crystal compared to the ZnS one, the slope efficiency is higher: almost 17%.

Anyway, larger efficiency associated to ZnSe crystal will drive us to reach better results in pulse duration rather than ZnS ones.

CW output power vs incident power for ZnSe with 3 percent output coupler.

Pump (W)	3 % O.C. (mW)
0.22	5
0.636	62
1.13	145
1.66	260
2.21	365
2.7	465
3.2	563
3.62	625
4.15	680
4.67	765
5.3	820

Table 3.2: CW output power vs incident power for ZnSe with 3 percent output coupler.

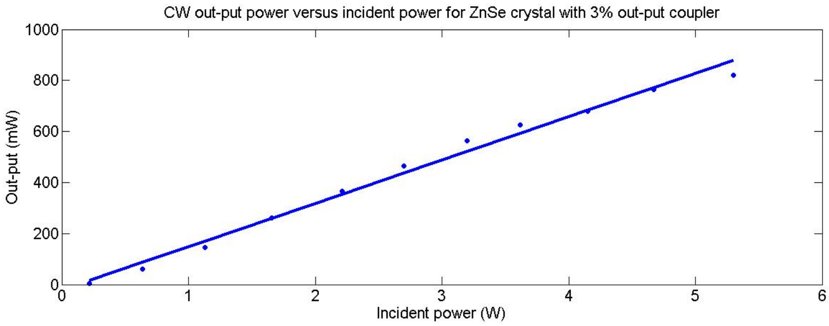

Figure 3.2: CW output power vs incident power for ZnSe with 3 percent output coupler.

3.1.2 Kerr-lens mode-locking configuration

Our goal is to get a stable mode-locking, with the shortest pulse duration possible, trying to maintain a pretty high average power. Next plots will compare CW regime with ML regime for each crystal in terms of average power and slope efficiency. The cavity to refer at is the 250 MHz one with 3% output power for both the crystals.

Tab.3.3 and Fig. 3.3 refers to the mode-locking regime power characteristics for the ZnS crystal, highlighting the comparison with the previous CW case. Average power is lower, with a low value of slope efficiency. Furthermore, no mode-locking action can be found for input power lower than 2 W, so we can assume this value as threshold.

CW vs ML comparison for ZnS with 3 percent output coupler

Pump (W)	**3 % O.C. (mW)**
2.1	131
2.8	203
3.5	235

Table 3.3: CW vs ML comparison for ZnS with 3 percent output coupler.

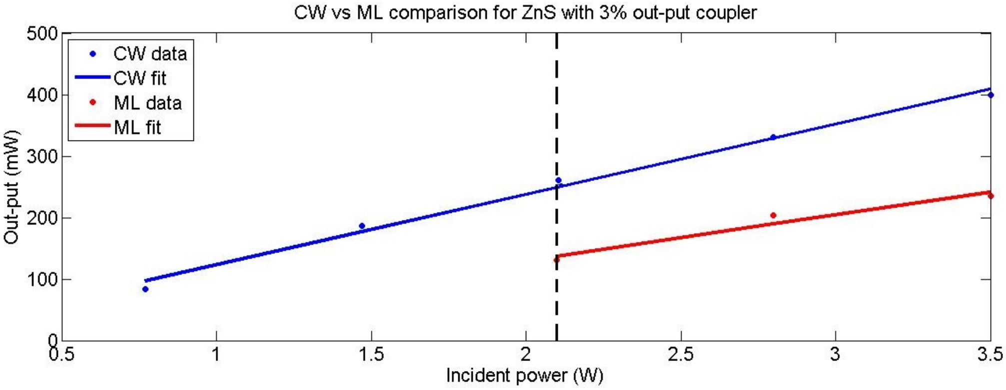

Figure 3.3: CW vs ML comparison for ZnS with 3 percent output coupler.

Tab.3.4 and Fig. 3.4 show mode-locking data for ZnSe: here we can notice the almost flat slope efficiency for ML characteristics in Fig. 3.4. Also in this case, mode-locking can start only with pump power greater than 2 W.

CW vs ML comparison for ZnSe with 3 percent output coupler

Pump (W)	**3 % O.C. (mW)**
2.21	169
2.7	172
3.2	174
3.62	180
4.15	188

Table 3.4: CW vs ML comparison for ZnSe with 3 percent output coupler.

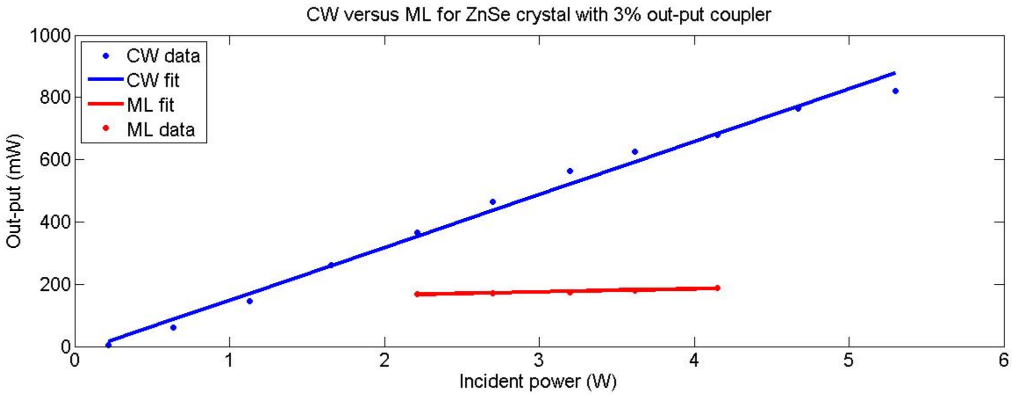

Figure 3.4: CW vs ML comparison for ZnSe with 3 percent output coupler.

3.2 Output pulse characteristics

Here we've finally reached the purpose of our analysis. Pulse characteristics is the aim of working in a mode-locking regime, and pulse duration together with pulse spectrum and spatial profile are the main issues to take into account for most applications. Starting with pulse duration measurements first, we'll introduce the theory behind autocorrelation and in particular the FRAC autocorrelation set-up we used.

3.2.1 Two photon non-linear absorption autocorrelation

Autocorrelation methods usually exploit SHG in a non-linear crystal in order to retrieve pulse duration. Input pulse is split into two components and to one of these a time-dependent delay is added. Both pulses recombine inside the non-linear crystal that, due to their interference at the surface and to the SHG related to this interference, will give an output beam with a pulse shape that can be easily measured by a photomultiplier tube and lead back to the input pulse shape and its duration (thanks to a factorial conversion). This dynamics is actually quite expensive, and for this reason two-photon absorption autocorrelation (TPA) become more attractive. TPA is the simultaneous absorption of two photon of different (or even equal) frequencies in order to excite a molecule from the ground state to an excited one with energy equal to the sum of the two photons energies. It is a third order non-linear effect and, for this reason, it is proportional to the square of the intensity beam: this means that is quite irrelevant for low intensity but quite strong for high ones. This non-linearity due to the semiconductor directly inside the detector can cover the role of the non-linear crystal in the second harmonic autocorrelator, overcoming all the problems of phase-matching inside the crystal and giving also an easier alternative to more complicated methods like Frequency Resolved Optical Gating (FROG) [41]. TPA autocorrelator is in facts more convenient in terms of costs, sensitivity and set-up adjustments (for SHG method a fine tuning of the crystal angle depending on the wavelength is needed in order to get the phase matching for non-linear effect) [42]. This solution uses semiconductor photodetectors where the large bandgap is an important requirements in order to extend the detection also for shorter wavelength like ultraviolet region [43]. Anyway, for our case, it's enough a relatively small band-gap that will allow to detect near-infrared wavelength. Two photon response of the autocorrelator is proportional to the product of both peak and average power of the input beam [44], and for this reason sensitivity is usually defined as the product of average power and peak power of the minimum signal detectable.

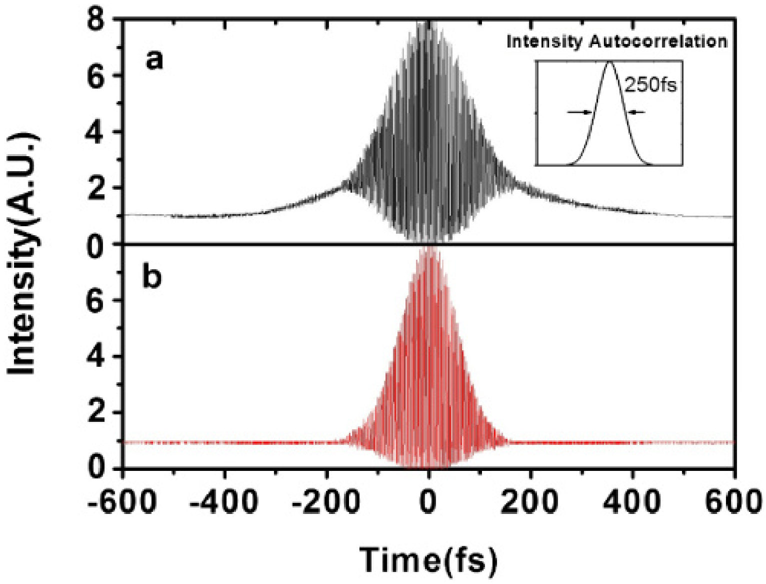

Figure 3.5: Autocorrelation signal: upper figure refers to a chirped pulse measurement; lower figure to an unchirped one.

The simplest interferometric signal is the one retrieved by a linear detector that records the intensity of the two recombined pulses [45]. Remembering that the the two pulses have the same electric field because they are the copy of the same input pulse passing through the beam splitter, the measured signal can be written as

$$S_{linear} = \int_{-\infty}^{+\infty} [E(t) + E(t+\tau)]^2 dt = 2\int_{-\infty}^{+\infty} I(t)dt + 2\int_{-\infty}^{+\infty} E(t)E(t+\tau)dt \quad (3.1)$$

where the first term is the offset given by the summed intensities of the two pulses and the second one is the interference term (or autocorrelation term). Nevertheless, a linear autocorrelation has no information beyond total pulse's intensity and spectrum's amplitude, and this constitutes a problem since we're interested to retrieve useful information about pulse duration. The common solution is to use a non linear detector that is sensitive to the squared signal intensity:

$$S_{quadratic} = \int_{-\infty}^{+\infty} \left\{[E(t) + E(t+\tau)]^2\right\}^2 dt \tag{3.2}$$

Substituting the E field with $E(t) = Re[A(t)e^{i\phi_a(t)}e^{i\omega_0 t}]$ and defining S_0 as $S_0 = \int_{-\infty}^{+\infty} A^4(t)dt$ to be able to normalize we obtain

$$S_{quadratic} = \frac{1}{S_0}(S_{f_0} + S_{f_1} + S_{f_2}) \tag{3.3}$$

where

$$S_{f_0} = \int_{-\infty}^{+\infty} [A^4(t) + 2A^2(t)A^2(t+\tau)]dt, \tag{3.4}$$

$$S_{f_1} = 2Re\left\{e^{i\omega_0\tau}\int_{-\infty}^{+\infty} A(t)A(t+\tau)[A^2(t) + A^2(t+\tau)]e^{i[\phi_a(t+\tau)-\phi_a(t)]}dt\right\}, \tag{3.5}$$

$$S_{f_2} = Re\left[e^{i2\omega_0\tau}\int_{-\infty}^{+\infty} A^2(t)A^2(t+\tau)e^{i2[\phi_a(t+\tau)-\phi_a(t)]}dt\right] \tag{3.6}$$

S_{f_0} is the intensity correlation with background (the so-called frequency component $\omega = 0$ of $S_{quadratic}$), S_{f_1} is the sum of two symmetric cross-correlation and it is phase dependent (frequency component $\omega = \pm\omega_0$) and the last term S_{f_2} (frequency component $\omega = \pm 2\omega_0$) is the autocorrelation of second harmonic field and it is related to the second-harmonic spectrum intensity.

This means physically that, by moving the delay, electrical fields of both the pulses will influence reciprocally and the output signal, that is proportional to the integral of the modulus square, will present oscillations due to the constructive or destructive interference. The biggest bell shape is for $\tau = 0$ and it has a relative contrast of 8:1, analytically calculated by

$$\frac{S_{quadratic}(0)}{S_{quadratic}(\infty)} = \frac{\int_{-\infty}^{+\infty}(E+E)^4 dt}{\int_{-\infty}^{+\infty} E^4 dt + \int_{-\infty}^{+\infty} E^4 dt} = \frac{16\int_{-\infty}^{+\infty} E^4 dt}{2\int_{-\infty}^{+\infty} E^4 dt} = \frac{8}{1} \tag{3.7}$$

Fig. 3.5 shows the case of unchirped pulse measurement. For the chirped one we can notice the presence of tails for bigger delay. This is due to fact that, if the pulses are chirped (so different frequencies that compose the pulse are delayed spatially), for big delay τ there won't be interference between different colors (wavelengths).

For Gaussian pulses affected by limited bandwidth the FWHM of this kind of interferometric autocorrelation signal is related to the pulse duration by

$$\frac{\Delta t_{quadratic}}{\Delta t} = 1.6963 \tag{3.8}$$

Our experimental set-up is made by a 50% beam splitter that divide into to components the input mode-locked laser and drive each of the two pulses into two different (but almost equals in length) paths. The first pulse bounce into a fixed mirror, the other one into a mirror glued on a mechanical slide controlled by a waveform generator that, giving a triangular input signal at frequency 20 Hz, make the slide cover a back and forth travel in space, giving the time-dependent delay to the pulse. Both of them recombine into the beam splitter, focusing into the InGaAs detector thanks to a focal lens (Fig. 3.6).

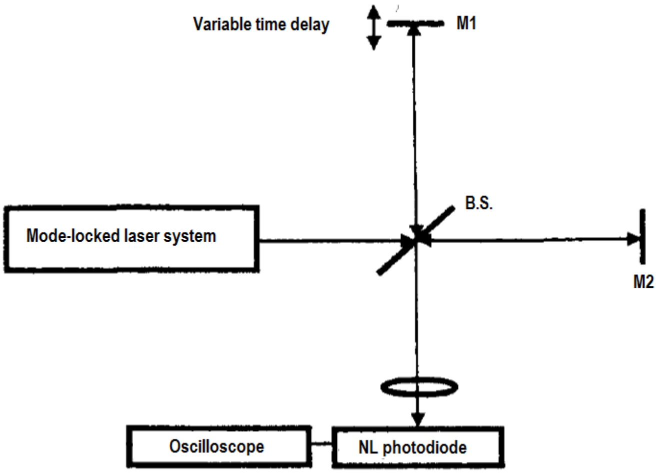

Figure 3.6: Typical experimental set-up for two photon autocorrelator. B.S. is a 50% beam splitter. Copyright [44]

3.2.2 Spectrum

Spectrum is essential to characterize pulse regime. As shown in Eq. 1.8 (frequency domain description), pulse duration has an inverse proportionality with the FWHM. This FWHM can be measured looking at the spectrum profile: larger bandwidth will correspond to shorter pulses. All the data have been taken from a NIRQuest 512-2.5 (Fig. 3.7) that operates between 900-2500 nm with a resolution of ∼6.3 nm.

Here below spectra belonging to ZnS and ZnSe crystals will be analyzed, underlining the difference in bandwidth between different set-ups.

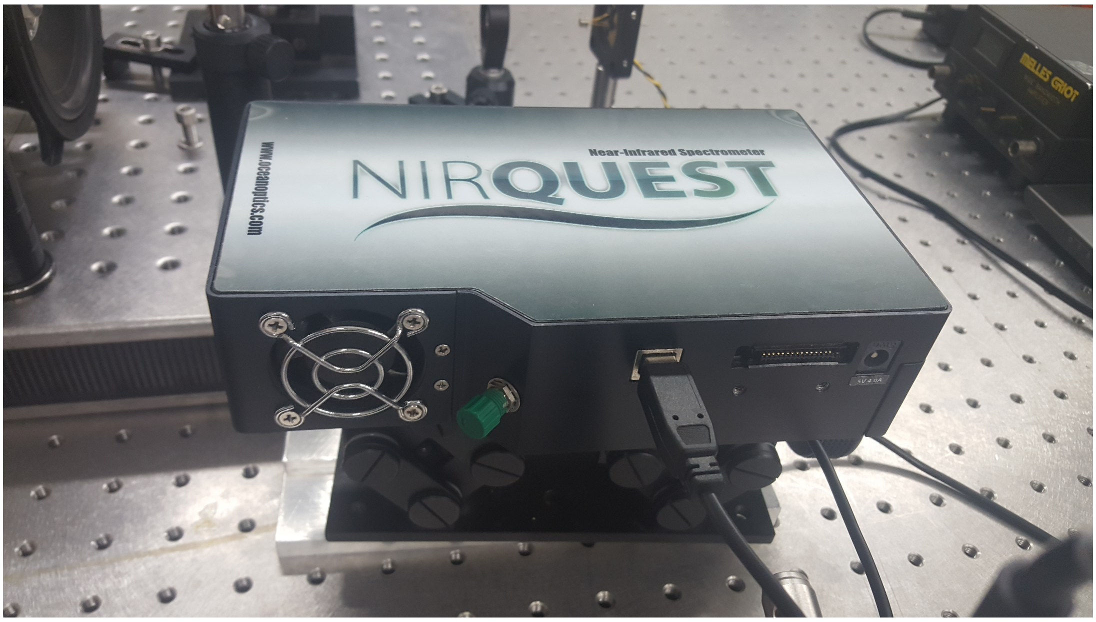

Figure 3.7: NIRQuest 512-2.5.

ZnS crystal

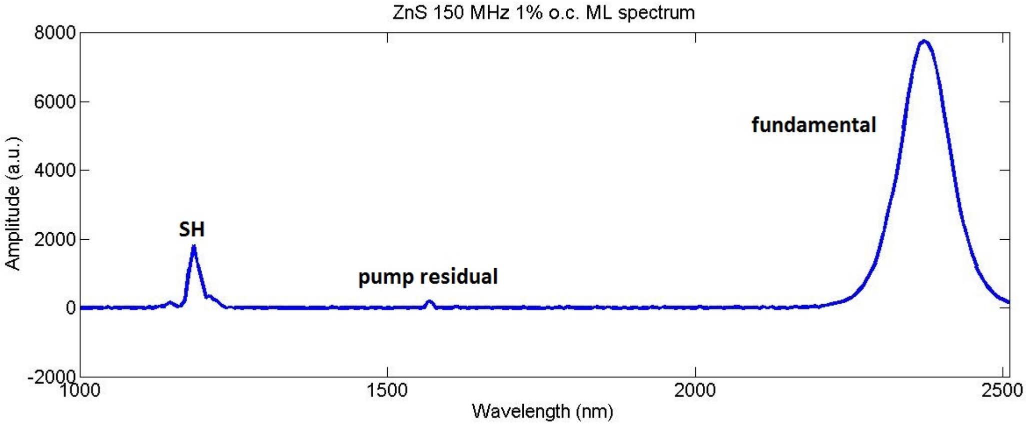

Figure 3.8: Spectrum for ZnS crystal. 150 MHz of repetition rate and 1% output coupler.

ZnS crystal, as we anticipated in Chapter II, uses to emits around 2300-2400 nm. In this first data plot (Fig. 3.8) we can notice the presence of an attenuated pump beam (around 1550 nm) and a heavy second harmonic generation (SHG) around half laser wavelength (1200 nm). ZnS is in fact well known for its hight third order non-linear coefficient and this allows to generate not only second harmonic, but also third or even forth ones.

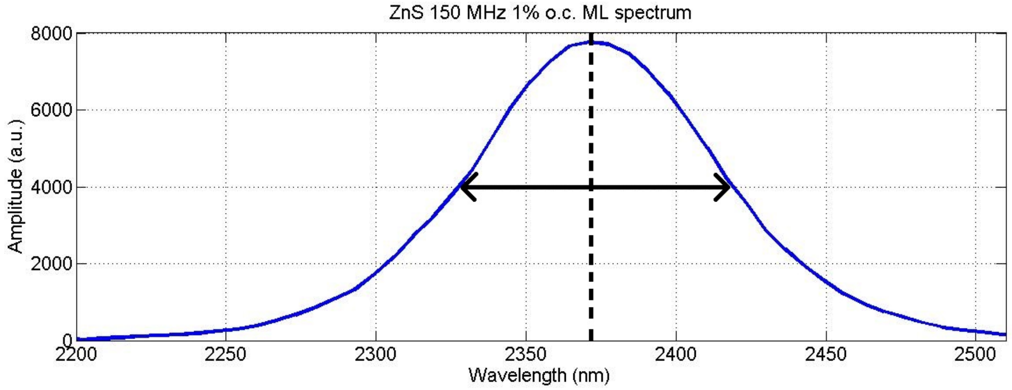

Figure 3.9: Spectrum detail for ZnS crystal. 150 MHz of repetition rate and 1% output coupler.

The quite large bandwidth can be appreciated in the detail of Fig. 3.9 and results to be almost 100 nm, centered at 2375 nm wavelength. For a more focused analysis about pulse duration it's necessary to measure the autocorrelation, but with these data we can estimate that it could be in the order of dozens of femtoseconds.

3% output coupler spectrum (Fig. 3.10) is a little bit different.

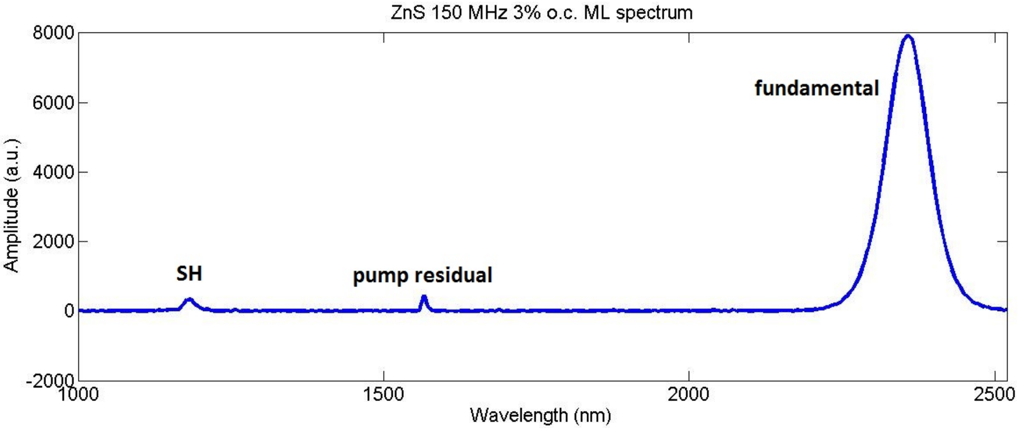

Figure 3.10: Spectrum for ZnS crystal. 150 MHz of repetition rate and 3% output coupler.

The repetition rate is always 150 MHz and the presence of pump and second harmonic is still visible, but the wavelength is a little bit shorter than the other case (∼2350 nm).

Also the bandwidth is smaller (Fig. 3.11), leading to a longer pulse duration. This is probably an effect of the less laser power trapped inside the resonator due to the bigger losses introduced with the higher transmission percentage of the new output coupler (3%) compared with the previous one (1%).

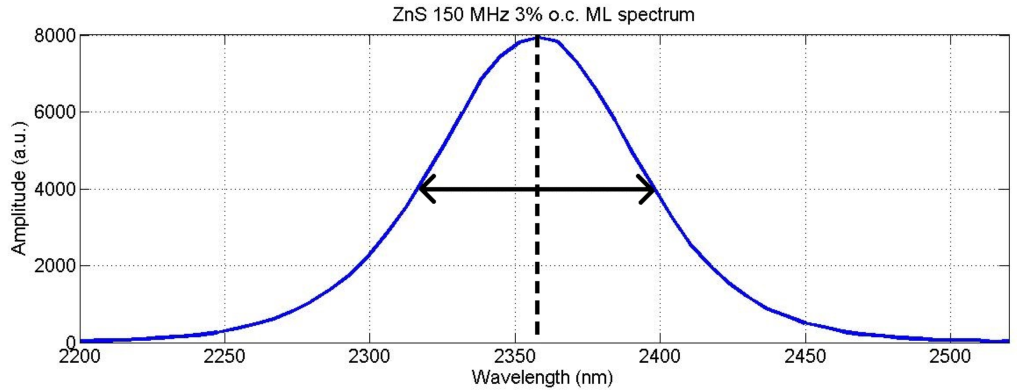

Figure 3.11: Spectrum detail for ZnS crystal. 150 MHz of repetition rate and 3% output coupler.

Last case is the 250 MHz one. Pump and second harmonic are not visible (Fig. 3.12) probably due to the different configuration that drive them to a different angled output not aligned with the OMA.

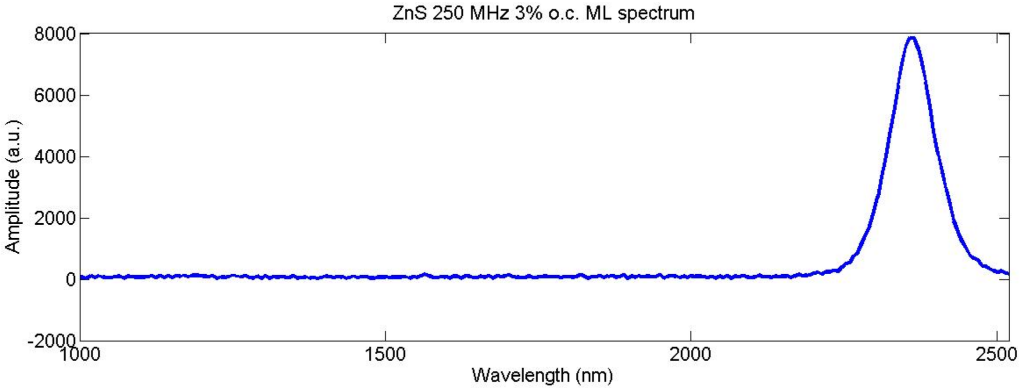

Figure 3.12: Spectrum for ZnS crystal. 250 MHz of repetition rate and 3% output coupler.

Bandwidth (Fig. 3.13) is larger than the previous case but still less than 100 nm. This slight increase for the 3% o.c. case is probably due to the more compact cavity, and for this reason we could expect that 1% o.c. 250 MHz configuration is the more efficient in terms of bandwidth. Anyway, since we're also looking for a good output power characteristics, this case won't be threaten.

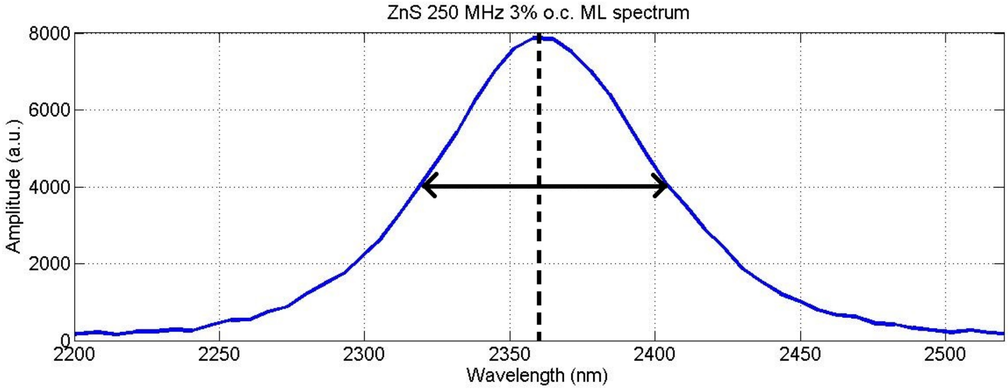

Figure 3.13: Spectrum detail for ZnS crystal. 250 MHz of repetition rate and 3% output coupler.

ZnSe crystal

ZnSe crystal has a shifted emission towards longer wavelength, usually 2400-2500 nm. All the previous bandwidth analysis has been done also for this crystal, comparing 1%, 3% and both 150 and 250 MHz laser configuration.

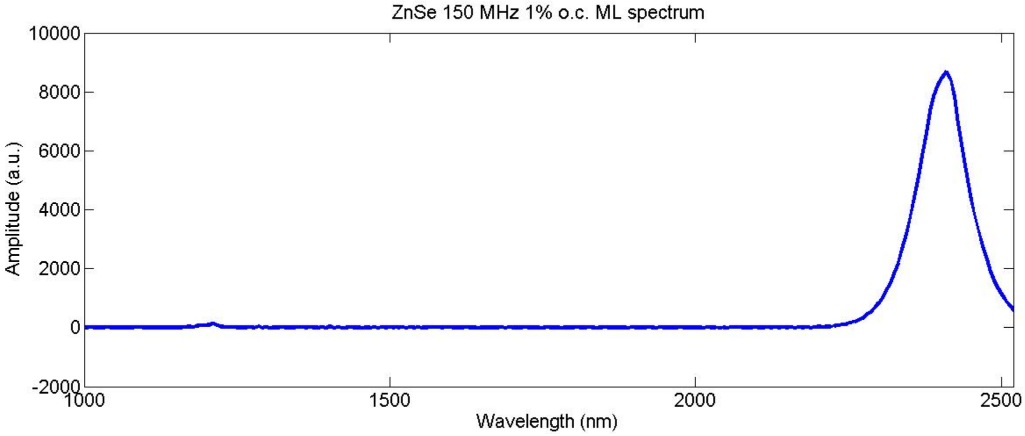

Figure 3.14: Spectrum for ZnSe crystal. 150 MHz of repetition rate and 1% output coupler.

Fig. 3.14 (whose detail is shown in Fig. 3.15) refers to 1% output coupler 150 MHz configuration for the ZnSe crystal, and it's possible to see the weak, but anyway present, second harmonic generation effect around 1250 nm. Wavelength is almost 100 nm red-shifted compared to the ZnS case (in facts it is around 1450 nm) and bandwidth is less than 100 nm.

3% output coupler case for 150 MHz repetition rate (Fig. 3.16) is slightly different: wavelength is centered around 2400 nm and the bandwidth is definitely

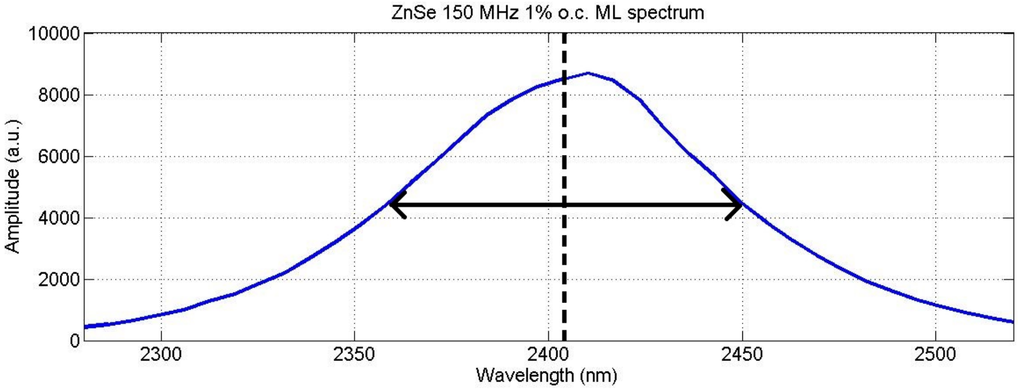

Figure 3.15: Spectrum detail for ZnSe crystal. 150 MHz of repetition rate and 1% output coupler.

larger than any other previous case (Fig. 3.17). With its ∼150 nm of bandwidth this configuration seems to be the more promising.

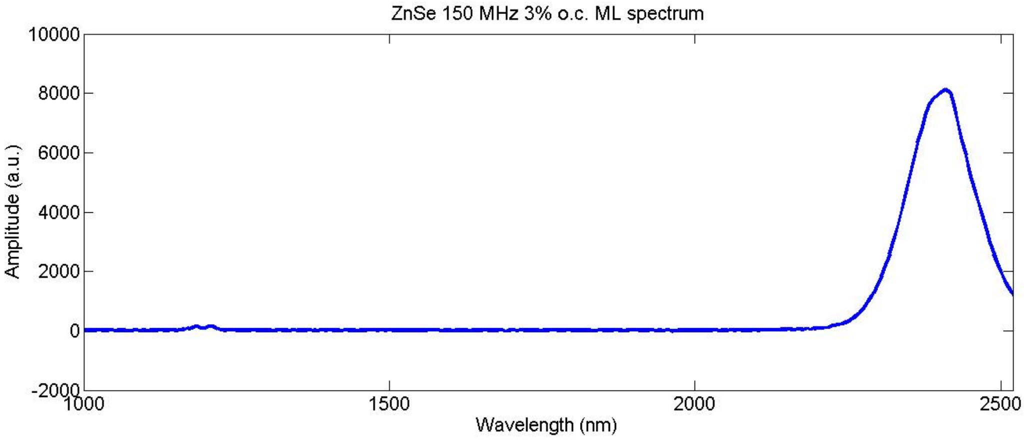

Figure 3.16: Spectrum for ZnSe crystal. 150 MHz of repetition rate and 3% output coupler.

As shown in the first picture, also second harmonic generation seems to reflect this large bandwidth, showing two different peaks.
3% o.c. give also the possibility to achieve higher power compared to 1% one and this, together with the broad-band, is the main reason why this configuration is still active in our laboratory.
With both nitrogen purging and fine management of third order dispersion (TOD) this configuration can be further improved.

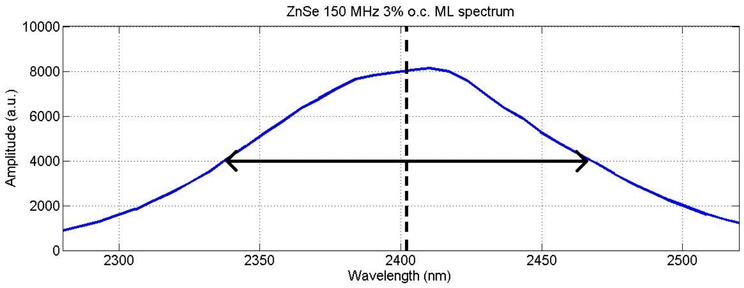

Figure 3.17: Spectrum detail for ZnSe crystal. 150 MHz of repetition rate and 3% output coupler.

Analogously to ZnS case, also 250 MHz configuration has been tested (Fig. 3.18). Bandwidth is slightly narrower (Fig. 3.19) than 150 MHz 3% output coupler (probably around 130 nm) and wavelength is centered in 2400 nm.

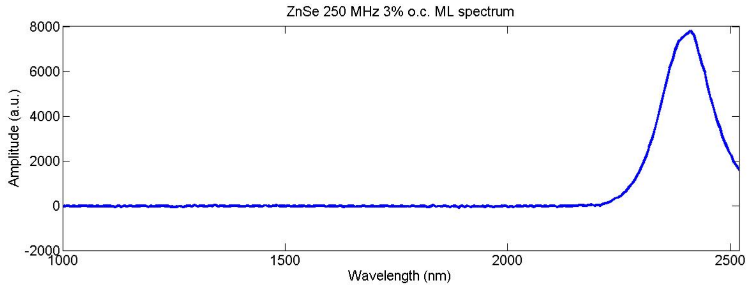

Figure 3.18: Spectrum for ZnSe crystal. 250 MHz of repetition rate and 3% output coupler.

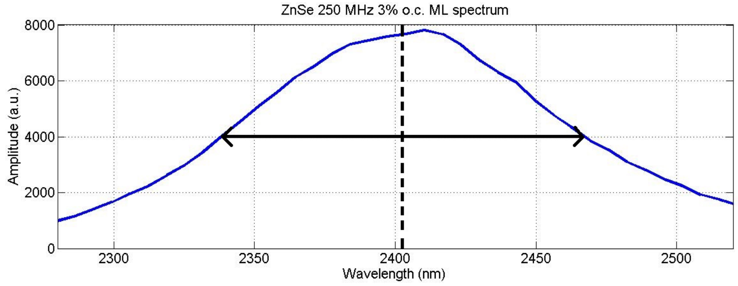

Figure 3.19: Spectrum detail for ZnSe crystal. 250 MHz of repetition rate and 3% output coupler.

For this particular crystal we organized all the best performances in a table (Tab. 3.5), measuring more accurately repetition rate and wavelength and giving also a better estimation for the bandwidth. Moreover, output power has been measured.

RESONATOR PARAMETERS	OUT-PUT POWER (mW)	CENTERED WAVELENGTH (nm)	BANDWIDTH (nm)
143 MHz, 1% o.c.	70	2410	90
143 MHz, 3% o.c.	300	2390	150
151 MHz, 3% o.c.	260	2410	130

Table 3.5: ZnSe performances.

Mode-locking performance

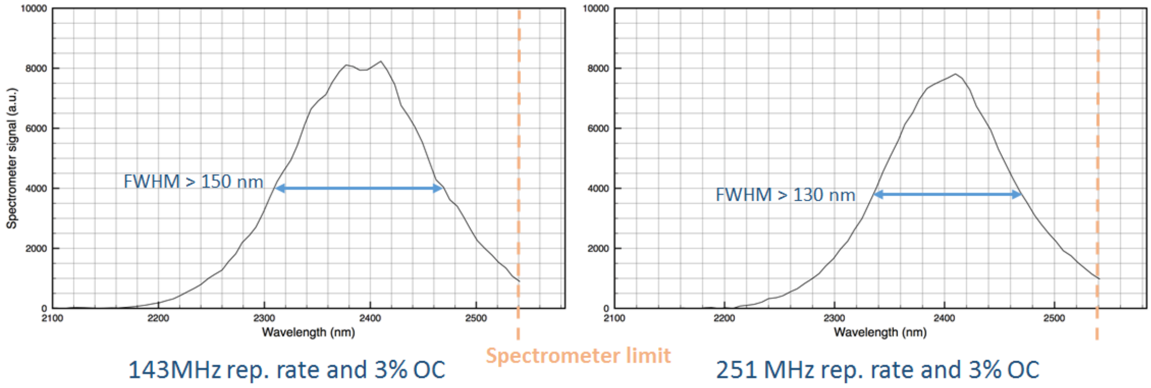

143MHz rep. rate and 3% OC

251 MHz rep. rate and 3% OC

Figure 3.20: ZnSe best performances for 150 and 250 MHz with 3% output coupler.

Fig. 3.20 shows in detail, with a fine grid, the spectra related to best performance for 150 and 250 MHz configuration with 3% output coupler.

3.2.3 Nitrogen purging effect

Has already anticipated in Chapter II, nitrogen purging has been tested in order to get the best performance. Results refer to the 250 MHz configuration with 3% o.c. in the case of ZnSe crystal. Initial centered wavelength is, in this case slightly different from the best performance, around 2380 nm. Set-up is shown in Fig. 3.21: laser is put inside the metal box, which has 2 holes allowing nitrogen flux to flow (inlet and outlet); spectrometer is placed inside too; a glass window for the incoming pump beam has been placed on the right side of the box.

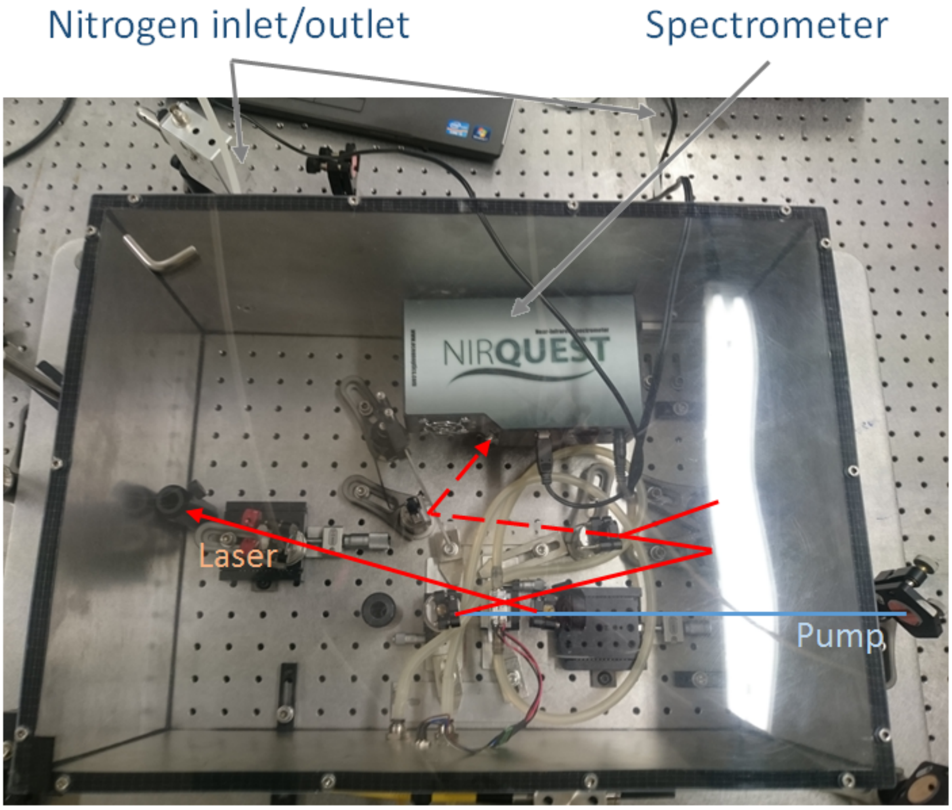

Figure 3.21: Nitrogen set-up.

Fig. 3.22 shows the influence of this nuance on the spectrum: reducing the relative humidity of the laser resonator environment leads to lower intra-cavity losses, and this will make achieve slightly higher performance. Quantifiable improvements are:

- slight increase of the output power
- red-shift of the peak wavelength
- slight broadening of the spectrum

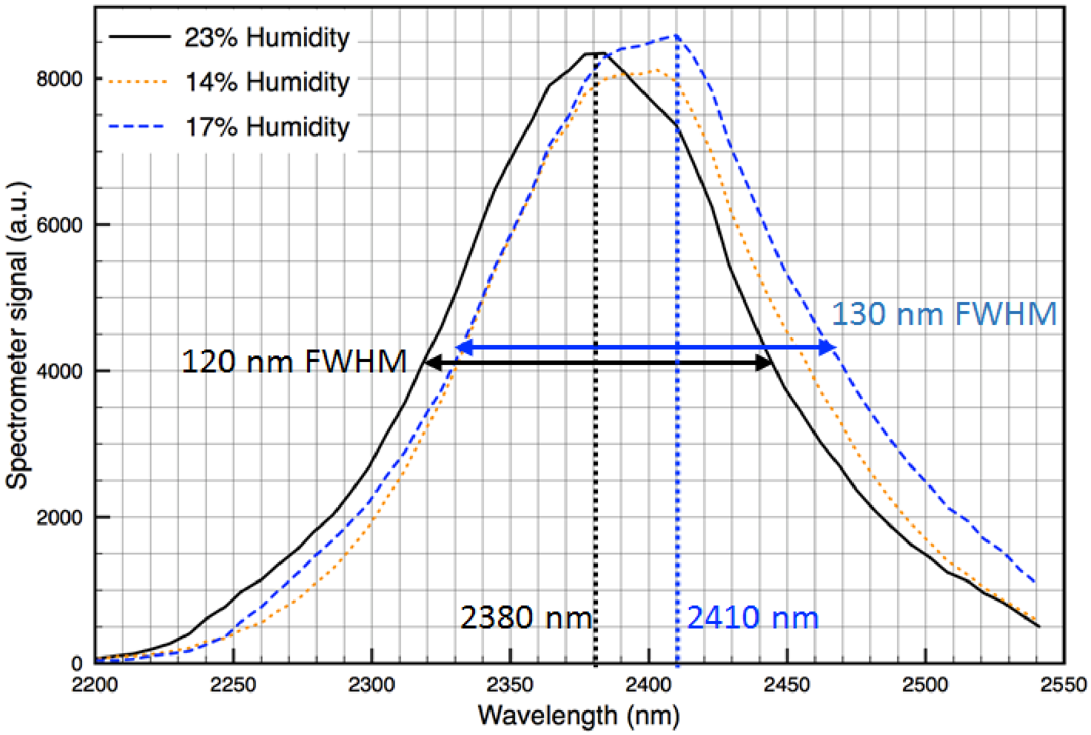

Figure 3.22: Nitrogen effect on the spectrum.

3.2.4 Spatial profile

For what concern the beam spatial profile we used a WinCamD-FIR2-16-HR from DataRay Inc. which gave us the possibility to fully characterize the spatial profile of our laser modes. The measurement has been taken on the ZnSe 150 MHz 3% output coupler laser configuration and for sure its shape can change depending on the different modes resonating inside the cavity. For us the best goal was to achieve a TEM_{00} mode, so we concentrated our efforts in order to optimize our output laser also from this point of view.

Anyway, Fig. 3.23 refers to the gaussian longitudinal mode of our laser that is, actually, a TEM_{10} mode. This elliptical shaped profile is due to the multi-mode regime of the beam propagating inside the cavity, along the horizontal axis.

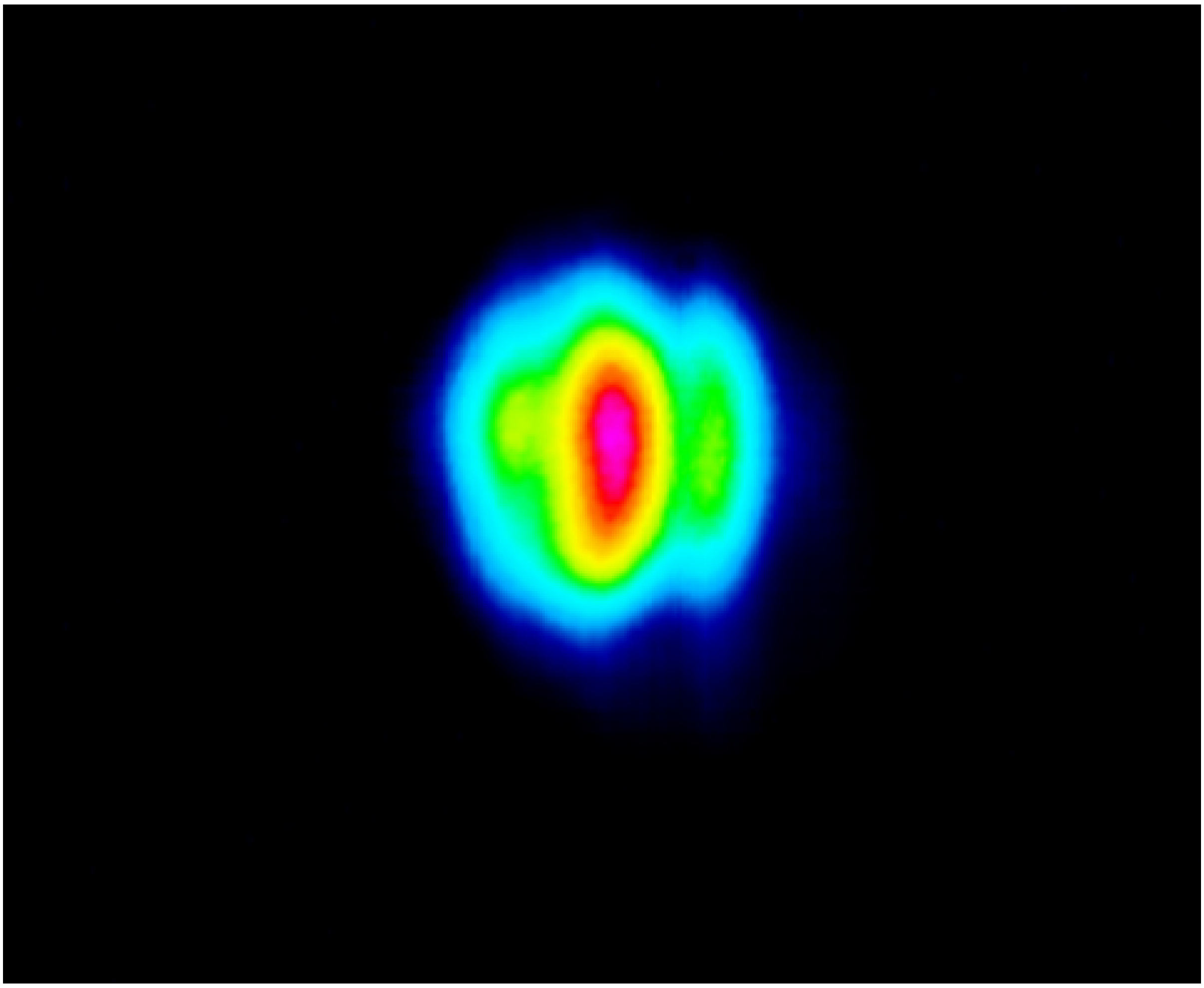

Figure 3.23: Spatial mode profile for ZnSe KLML with 3% o.c. and 150 MHz of repetition rate.

3.2.5 Pulse duration

Pulse duration is one of the last issue to estimate. We already analyzed two photon non-linear absorption in the beginning of this chapter end the experimental set-up is shown in Fig. 3.24.
Pulse time duration has been calculated measuring the fringe number at the half maximum of the autocorrelation shape, and than dividing it by a factor of two. In facts the two pulses' electric fields interfere passing through each others and the optical autocorrelation signal will last twice the duration of a single pulse. Then, each fringe of interference will correspond to a single electric field oscillation and to retrieve a single pulse duration (that is measured at its half maximum intensity amplitude) will be enough to multiply the single oscillation duration by the number of fringe interference.
For our wavelength (~2400 nm) the single oscillation time is $\tau_0 = \lambda/c$ (where c

is the speed of light) that is $\tau_0 = 8fs$.

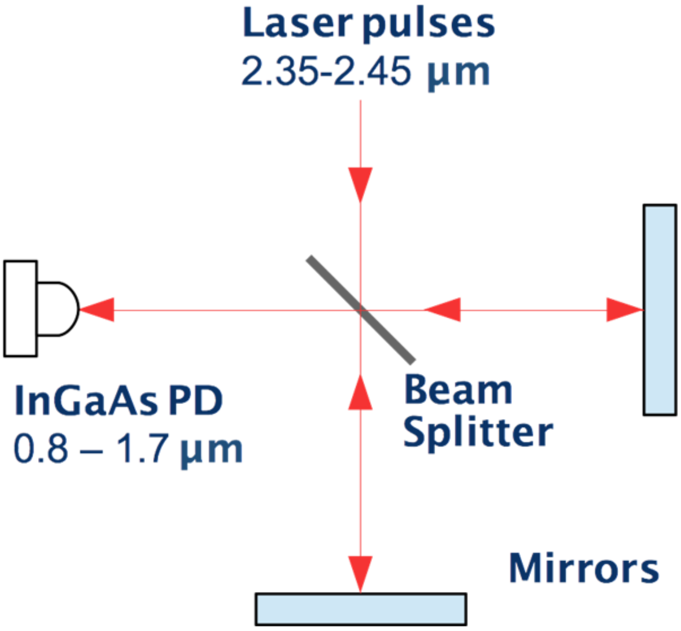

Figure 3.24: Experimental set-up for pulse duration estimation.

ZnS crystal

ZnS crystal was the first to be put on the testbed, and the next three figures show autocorrelation profile for each configuration. Signal to noise ratio is not optimized in particular for the first measure and this dependence may be due to the focal length of the lens.

Fig. 3.25 refers to 150 MHz 1% o.c. and as we can see the number of fringes is approximately 10. Single electric field oscillation for ZnS is slightly different because of its shorter wavelength, so we can estimated it equal to $\tau_0 = 7.9$ fs. The results is a pulse duration close to $\tau_p = 10\tau_0 = 79fs$. Using relation $\Delta\lambda/\lambda_c = \Delta\nu/\nu_c$ (where Δ means the bandwidth and the subscript "c" means "central") that relate wavelength bandwidth to the frequency bandwidth we can calculate the time-bandwidth product and compare it to the transform limit for $sech^2$ profile pulse, that is 0,315. In our case we can assume $\Delta\lambda = 100nm$ that makes $\Delta\nu = \nu_c\Delta\lambda/\lambda_c = c\Delta\lambda/\lambda_c^2 = 5,3$ THz. In the end $\Delta\nu\tau_p \sim 0,418 > 0,315$ which is the theoretical value. This means that we are close to the theoretical limit, but this is not the shortest pulse duration possible.

Fig. 3.26 and Fig. 3.27 refer to the other two configurations, and all values are shown in Tab. 3.6. For all the three configurations we can say we're not

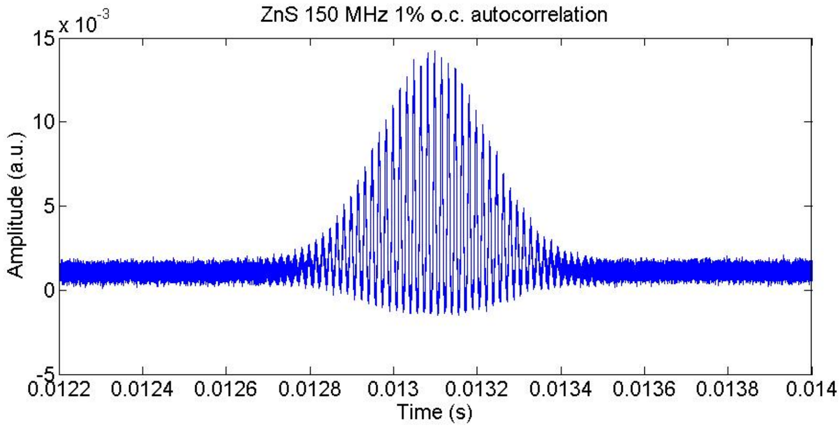

Figure 3.25: Autocorrelation for ZnS crystal. 150 MHz of repetition rate and 1% output coupler.

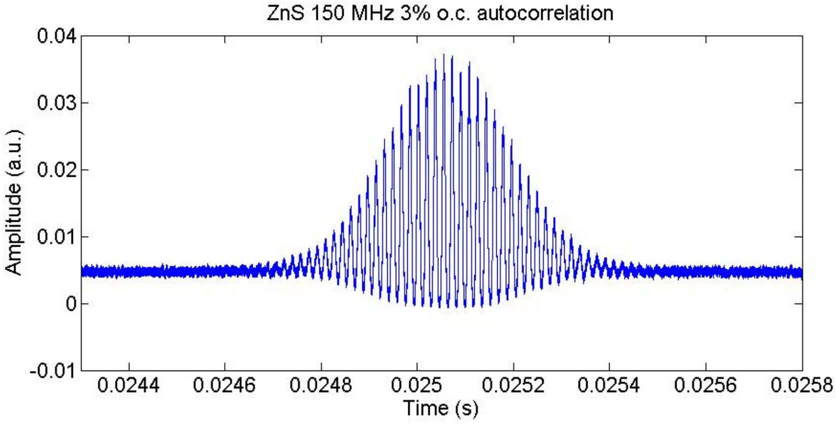

Figure 3.26: Autocorrelation for ZnS crystal. 150 MHz of repetition rate and 3% output coupler.

limited by chirp because we have no deformation at trailing and leading edges of autocorrelation profile.

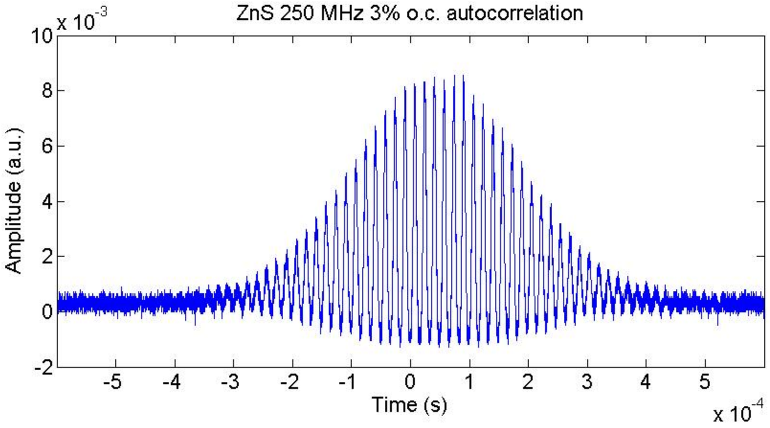

Figure 3.27: Autocorrelation for ZnS crystal. 250 MHz of repetition rate and 3% output coupler.

Configuration	λ_c (μm)	$\Delta\lambda$ (nm)	$\Delta\nu$ (THz)	**# fringes**	τ_p (fs)	**Transform limit**
150MHz-1%	2375	100	5,3	10	79	0,418
150MHz-3%	2350	80	4,3	10	79	0,340
250MHz-3%	2365	90	4,8	10	79	0,379

Table 3.6: Values derived from autocorrelation for the three ZnS configurations.

ZnSe crystal

ZnSe was the most promising for what concern large bandwidth, and for sure more interesting to analyze. Signal to noise ratio, for this case, is really high as it is possible to appreciate in Fig. 3.28, Fig. 3.29 and Fig. 3.30. This is because of the new lens we used to make the beam focus inside the InGaAs detector. First figure refers to 150 MHz 1% o.c. configuration and, although it is the worst case compared to the other two cases, S/N is much higher than ZnS case. Moreover, no one of these configuration, as the previous three, is visibly chirped.

Configuration	λ_c (μm)	$\Delta\lambda$ (nm)	$\Delta\nu$ (THz)	**# fringes**	τ_p (fs)	**Transform limit**
150MHz-1%	2410	100	5.1	8	64	0,327
150MHz-3%	2390	150	7,8	6	48	0,375
250MHz-3%	2410	130	6,7	7	56	0,375

Table 3.7: Values derived from autocorrelation for the three ZnSe configurations.

All data are calculated as shown in ZnS paragraph and can be found in Tab. 3.7.

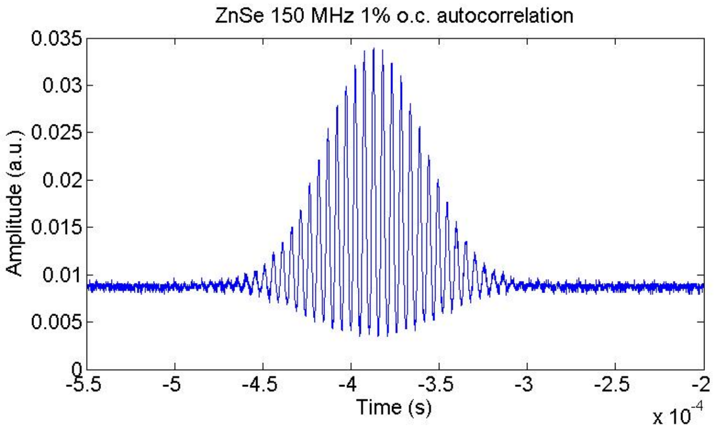

Figure 3.28: Autocorrelation for ZnSe crystal. 150 MHz of repetition rate and 1% output coupler.

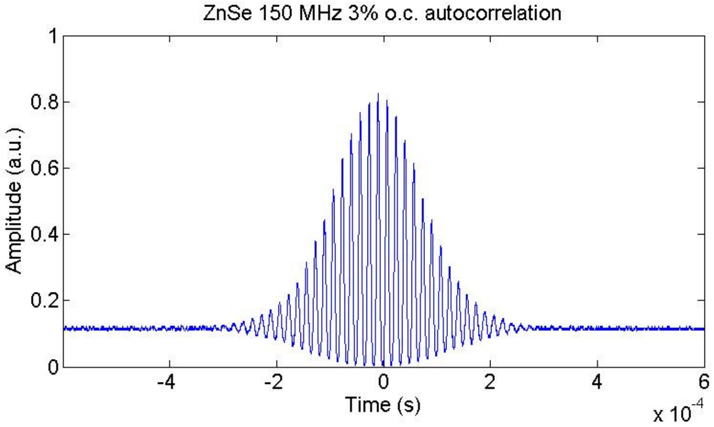

Figure 3.29: Autocorrelation for ZnSe crystal. 150 MHz of repetition rate and 3% output coupler.

For what concern the transform limit we can observe that the most of our configurations generate larger pulses compared to those that transform limit condition allows. This could be due to two main issues: the former is the GVD compensation that could have given a strong negative chirp; the latter is the chirp added by the output coupler that could contaminate our measurements. Both of them are a purely set-up issue, that can be fixed adopting chirped mirrors with more appropriated specifications.

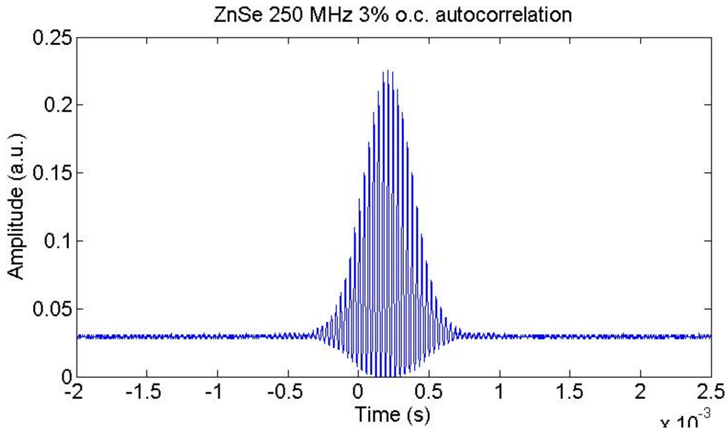

Figure 3.30: Autocorrelation for ZnSe crystal. 250 MHz of repetition rate and 3% output coupler.

3.3 Relative intensity noise measurements

Being an imperfect optical oscillator, laser electric fields are affected by intensity and frequency noises. Particles nature of light and in particular discontinuous behavior of absorption and emission transitions is the origin of these noises [46] that can be generated also from cavity vibrations, fluctuations in the active medium or even transferred to the output from the pump source. Any kind of intensity oscillation is reflected into a limit for all possible optical communications and such oscillations are even present in the most stable CW lasers. The parameter used to quantify these oscillation is known as RIN (Relative Intensity Noise). This parameter describes in facts the laser power level instability. Being the intensity noise an intensity dependent effect, RIN is not intensity dependent. The typically RIN shape is characterized by a peak at relaxation oscillation frequency of the laser and by a damping for higher frequencies that drive it to the shot noise level.

Before talking about this measurement applied to ZnSe 150 MHz with 3% o.c. configuration, let's have a brief re-calls on intensity fluctuations that affect optical sources.

Photo-current fluctuations' noise spectral density is, at the detector output, is

$$w_{\Delta I}(f) = 2qI_{ph} + I^2 RIN(f) \tag{3.9}$$

where

$$RIN(f) = \frac{W_{\Delta J}(f)}{< I >^2} \tag{3.10}$$

I_{ph} is the output average photo-current, q the electronic charge, $< I >$ the optical field average intensity and $W_{\Delta J}(f)$ is the intensity fluctuations' power spectral density. The first term of 3.9 is the shot noise and it's highlight the discontinuous nature af photons and electrons. The second one presents the term RIN: this is a term referring to the source, and for this reason we should analyze source rather then detector properties if we need to known more about it.

Experimental set-up and measurements

Many different approaches can be followed in order to measure RIN, like the cross-spectrum method that can be found in Ref. [47]. We used anyway a classical approach, with two different photodetector positions in order to measure both the pump and the output laser. Fig. 3.32 gives an idea of the experimental set-up.

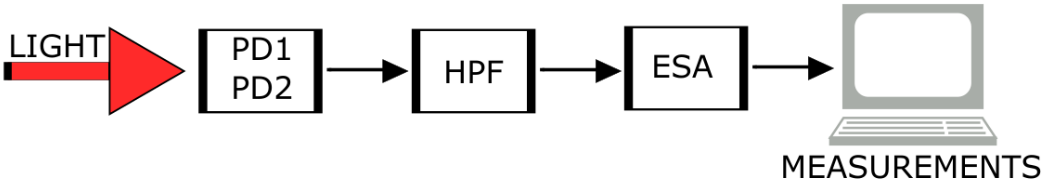

Figure 3.31: Block diagram of the set-up for RIN measurements.

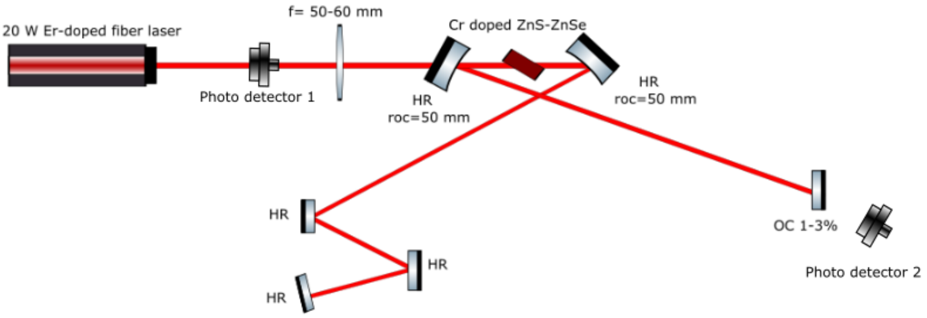

Figure 3.32: Position of photodetectors for RIN measurements.

Fig. 3.31 shows the block diagram for the measurements: light is detected by the photodetector in position 1 for the pump or in position 2 for the output ZnSe laser, then the signal pass through an high pass filter and, in the end, an electric spectrum analyzer collect the data and make the fast fourier transform of the time-varying signal, showing the classical $RIN(f)$ function.

Let's analyze Fig. 3.33 first, which refers to the pump intensity oscillations. Black line is the the noise of the detector when no light is impinging it. Red line is the effective measurement and it's possible to appreciate that it stays always above the black one, indicating that all our "noise" measurements are due to the incoming light and not to the detector noise. First of all we can recognize a $1/f$ noise in the low frequencies range, although it has probably a much more slope damping compared to the typical $1/f$ noise behavior. Central frequencies (between 10^2 and 10^4 Hz) are affected by white noise. Around 10^5 Hz it's also possible to see an overshoot followed by a dumping that drives the noise to the "shot noise" level for frequencies bigger than 10^6 Hz. In the end, before 10^7 Hz it's clearly visible a couple of peaks. This characterization refers to the Er:fiber laser and consequently all these noise are transferred to our output laser.

Fig. 3.34 shows in facts a similar behavior also for the ZnSe beam: $1/f$ noise

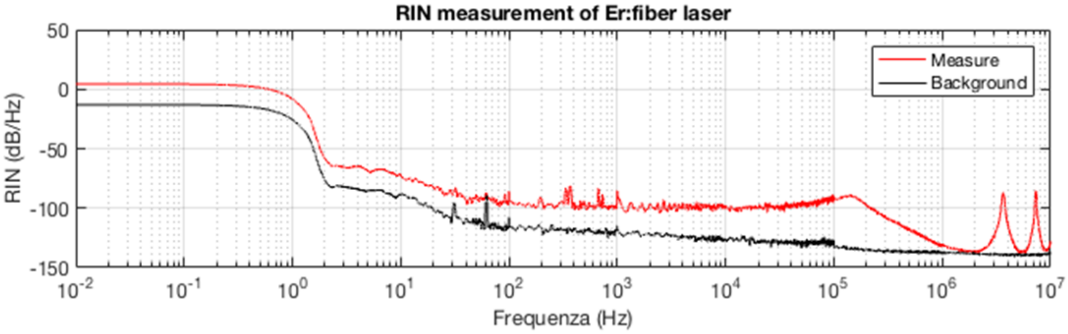

Figure 3.33: RIN measurement for the pump.

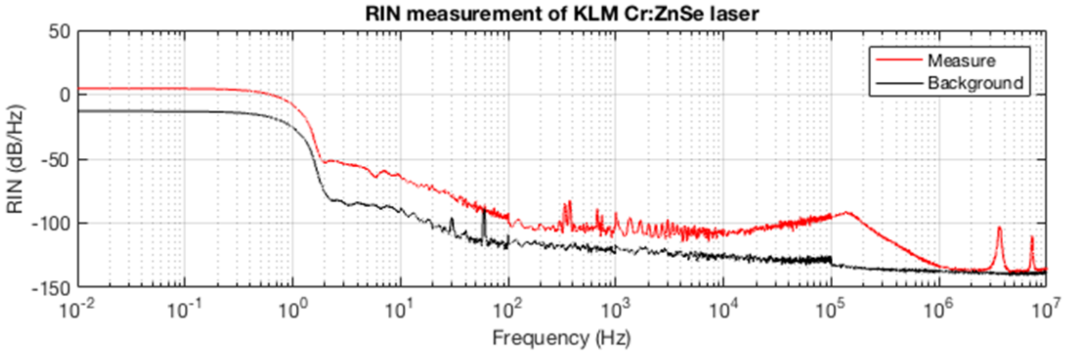

Figure 3.34: RIN measurement for the output ZnSe laser.

for low frequencies, white noise for central ones an overshoot around 10^5 Hz. The two peaks in the highest frequencies region are slightly smaller than the pump case and this suggests us that our laser filters, somehow, the pump noise, behaving like a band-pass filter with a shorter cut-off frequency. The $1/f$ noise is slightly amplified for low frequencies but it's possible to see that, for frequencies higher than 10^2 Hz, our noise is lower than -100 dB.

For sure we can say to have an oscillation noise definitely good because our noise is only due to the quite small pump noise, but this is also a limit for further improvements: if we want to reach better results, the only possible choice is to change the commercial pump laser.

Conclusion and perspectives

We described the design, the realization and the characterization of Kerr-lens mode-locked Cr-doped ZnS and ZnSe lasers. We demonstrated few optical cycles of pulse duration at around 2.4 μm in the case of ZnSe, reaching a good power efficiency. Comparing RIN measurements of the pump laser and of the Cr-doped lasers it appears that our commercial pump source is the main noise source of the developed mode-locked lasers. The laser, mounted on a compact board, can be easily transportable. With its 143 MHz repetition rate, 300 mW output power, 150 nm of bandwidth and 48 fs of pulse duration the $Cr^{2+} : ZnSe$ laser results to be a perfect candidate for operate in all those applications related to the generation of optical frequency combs in the mid-infrared region and high-resolution molecular spectroscopy. Further activities will be addressed to stabilize the repetition frequency reaching a final instability reduction of five order of magnitude and to use a non-linear fiber in order to further broaden the laser bandwidth and generate an octave spanning super-continuum to measure the carrier envelope offset frequency and to transform this fs laser into an optical frequency comb synthesizer.

Bibliography

[1] Orazio Svelto. *Principles of Lasers ——*, volume 10.1007/978-1-4419-1302-9. 2010.

[2] Z. G. Lu; S. A. Boothroyd; J. Chrostowski. Frequency comb generation by cascade cavity-enhanced four-wave mixing in a semiconductor optical amplifier. *Microwave and Optical Technology Letters*, 23, 1999.

[3] H.A. Haus. Mode-locking of lasers. *IEEE Journal of Selected Topics in Quantum Electronics*, 6, 2000.

[4] H.; Sahara A.; Tamura K. Nakazawa, M.; Kubota. Time-domain abcd matrix formalism for laser mode-locking and optical pulse transmission. *IEEE Journal of Quantum Electronics*, 34, 1998.

[5] S. McDuff, O.; Harris. Nonlinear theory of the internally loss-modulated laser. *IEEE Journal of Quantum Electronics*, 3, 1967.

[6] O. Harris, S.; McDuff. Theory of fm laser oscillation. *IEEE Journal of Quantum Electronics*, 1, 1965.

[7] A. Kuizenga, D.; Siegman. Fm and am mode locking of the homogeneous laser - part i: Theory. *IEEE Journal of Quantum Electronics*, 6, 1970.

[8] E. P. Ippen. Principles of passive mode locking. *Applied Physics B*, 58(3):159–170, 1994.

[9] W. Sibbett and J.R. Taylor. Passive mode-locking of the flashlamp pumped coumarin 522 dye laser. *Optics Communications*, 44(2):121 – 124, 1982.

[10] G.H.C. New. Mode-locking of quasi-continuous lasers. *Optics Communications*, 6(2):188 – 192, 1972.

[11] JLA Dubbeldam, JA Leegwater, and D Lenstra. Theory of mode-locked semiconductor lasers with finite absorber relaxation times. *Appl. Phys. Lett*, 70:1938, 1997.

[12] Hermann A. Haus. Theory of mode locking with a fast saturable absorber. *Journal of Applied Physics*, 46, 1975.

[13] AJ DeMaria, DA Stetser, and H Heynau. Self mode-locking of lasers with saturable absorbers. *Applied Physics Letters*, 8(7):174–176, 1966.

[14] N. Xiang; F. Lin; H.P. Li; H.F. Liu; W. Liu; W. Ji; S.J. Chua. Gan-based semiconductor saturable absorber mirror operating around 415 nm. *Thin Solid Films*, 515, 2007.

[15] T. Li; S.Z. Zhao; Z. Zhuo; Y.G. Wang; G.Q. Li. Passively mode-locked yvo4/nd:yvo4 composite crystal green laser with a semiconductor saturable absorber mirror. *Laser Physics Letters*, 6, 2009.

[16] H. A. Haus, J. G. Fujimoto, and E. P. Ippen. Analytic theory of additive pulse and kerr lens mode locking. *IEEE Journal of Quantum Electronics*, 28(10):2086–2096, Oct 1992.

[17] Ch.; Curley P. F.; Krausz F. Brabec, T.; Spielmann. Kerr lens mode locking. *Optics Letters*, 17, 1992.

[18] Ondřej Haderka. Influence of diffraction on hard-aperture kerr-lens mode locking. *Optics Letters*, 20, 1995.

[19] David Huang, Morrison Ulman, Lucio H. Acioli, Hermann A. Haus, and James G. Fujimoto. Self-focusing-induced saturable loss for laser mode locking. *Opt. Lett.*, 17(7):511–513, Apr 1992.

[20] Juan L. A. Martínez, Oscar E.; Chilla. Self-mode-locking of ti:sapphire lasers: a matrix formalism. *Optics Letters*, 17, 1992.

[21] P.; Svelto O. De Silvestri, S.; Laporta. The role of cavity dispersion in cw mode-locked dye lasers. *IEEE Journal of Quantum Electronics*, 20, 1984.

[22] Ch.; Krausz F. Brabec, T.; Spielmann. Limits of pulse shortening in solitary lasers. *Optics Letters*, 17, 1992.

[23] J. D.; Nelson L. E. Haus, H. A.; Moores. Effect of third-order dispersion on passive mode locking. *Optics Letters*, 18, 1993.

[24] N.A. Agrawal, G.P.; Olsson. Self-phase modulation and spectral broadening of optical pulses in semiconductor laser amplifiers. *IEEE Journal of Quantum Electronics*, 25, 1989.

[25] I.; Dreischuh A. Dimitrov, N.; Stefanov. Spie proceedings [spie xvi international school on quantum electronics: Laser physics and applications - nessebar, bulgaria (monday 20 september 2010)] 16th international school on quantum electronics: Laser physics and applications - tuning the pulse duration, spectral position, and bandwidth of femtosecond pulses by the beam's penetration in an intracavity prism. volume 7747, 2010.

[26] O. E.; Gordon J. P. Fork, R. L.; Martinez. Negative dispersion using pairs of prisms. *Optics Letters*, 9, 1984.

[27] N.; Schibli T.; Keller U.; Haus H. A.; Heine C.; Morf R.; Scheuer V.; Tilsch M.; Tschudi T. Kärtner, F. X.; Matuschek. Design and fabrication of double-chirped mirrors. *Optics Letters*, 22, 1997.

[28] Karapat; Spielmann Christian; Krausz Ferenc Szipocs, Robert; Ferencz. Chirped multilayer coatings for broadband dispersion control in femtosecond lasers. *Optics Letters*, 19, 1994.

[29] Igor; Mirov Mike; Mirov Sergey; Gapontsev Valentin Vasilyev, Sergey; Moskalev. Three optical cycle mid-ir kerr-lens mode-locked polycrystalline $cr^{2+} : zns$ laser. *Optics Letters*, 40, 11 2015.

[30] Irina T. Ebrahim-Zadeh, Majid; Sorokina. *[NATO Science for Peace and Security Series B: Physics and Biophysics] Mid-Infrared Coherent Sources and Applications —— Broadband Mid-Infrared Solid-State Lasers*, volume 10.1007/978-1-4020-6463-0. 2008.

[31] Renata Reisfeld and Christian K Jorgensen. *Lasers and excited states of rare earths*, volume 1. Springer Science & Business Media, 2012.

[32] H. J. Queisser. *[Advances in Solid State Physics] Festkörperprobleme 15 Volume 15 —— Lead salt laser diodes*, volume 10.1007/BFb0107371. 1975.

[33] Uwe Peter Schießl; J Rohr. 60 celsius degrees lead salt laser emission near 5-μm wavelength. *Infrared Physics and Technology*, 40, 1999.

[34] Chao Liu, Yanbo Li, Yiping Zeng, et al. Progress in antimonide based iii-v compound semiconductors and devices. *Engineering*, 2(08):617, 2010.

[35] Brian R Bennett, Richard Magno, J Brad Boos, Walter Kruppa, and Mario G Ancona. Antimonide-based compound semiconductors for electronic devices: A review. *Solid-State Electronics*, 49(12):1875–1895, 2005.

[36] Ralph H Page, Kathleen I Schaffers, Laura D DeLoach, Gary D Wilke, Falgun D Patel, John B Tassano, Stephen A Payne, William F Krupke, K-T Chen, and Arnold Burger. Cr/sup 2+/-doped zinc chalcogenides as efficient, widely tunable mid-infrared lasers. *IEEE Journal of Quantum Electronics*, 33(4):609–619, 1997.

[37] Richard Moncorgé. Laser materials based on transition metal ions. *Optical Materials*, 63:105–117, 2017.

[38] Sergey Vasilyev, Igor Moskalev, Mike Mirov, Sergey Mirov, and Valentin Gapontsev. Multi-watt mid-ir femtosecond polycrystalline cr 2+: Zns and cr 2+: Znse laser amplifiers with the spectrum spanning 2.0–2.6 μm. *Optics express*, 24(2):1616–1623, 2016.

[39] JT Vallin, GA Slack, S Roberts, and AE Hughes. Infrared absorption in some ii-vi compounds doped with cr. *Physical Review B*, 2(11):4313, 1970.

[40] Stefan Kück. Spectroscopy and laser characteristics of cr2+-doped chalcogenide crystals — overview and recent results. *Journal of Alloys and Compounds*, 341, 2002.

[41] Young Jae; Song Ho Seong; Kim Dug Young Chin, Sang Hoon; Kim. Complete chirp analysis of a gain-switched pulse using an interferometric two-photon absorption autocorrelation. *Applied Optics*, 45, 2006.

[42] H. K.; Day I. E.; Drake J.; Knights A. P.; Asghari M. Liang, T. K.; Tsang. Silicon waveguide two-photon absorption detector at 1.5 wavelength for autocorrelation measurements. *Applied Physics Letters*, 81, 2002.

[43] K.S Wong; T Sun; Bosco K.K Fung; I.K Sou; G.K.L Wong. Visible to ultraviolet femtosecond autocorrelation measurements based on two-photon absorption using znsse photodetector. *Journal of Crystal Growth*, 227-228, 2001.

[44] Jai-Hyung; Chang Joon-Sung; Lim Yong-Sik; Park Jong-Dae Noh, Young-Chul; Lee. Visible wavelength autocorrelation based on the two-photon absorption in a sic photodiode. *Journal of the Optical Society of Korea*, 3, 1999.

[45] Frank Träger. *Springer Handbook of Lasers and Optics Volume 1100 —— Lasers and Coherent Light Sources*, volume 10.1007/978-3-642-19409-2. 2012.

[46] Irène Joindot. Measurements of relative intensity noise (rin) in semiconductor lasers. *Journal de Physique III*, 2(9):1591–1603, 1992.

[47] Kirill; Larger-Laurent Rubiola, Enrico; Volyanskiy. [ieee 2009 joint meeting of the european frequency and time forum (eftf) and the ieee international frequency control symposium (fcs) - besancon, france (2009.04.20-2009.04.24)] 2009 ieee international frequency control symposium joint with the 22nd european frequency and time forum - measurement of the laser relative intensity noise. 2009.